Monthly Notices of the ROYAL ASTRONOMICAL SOCIETY

MNRAS **501,** 2430–2450 (2021) doi:10.1093/mnras/staa3812
Advance Access publication 2020 December 11

GLACE survey: Galaxy activity in ZwCl0024+1652 cluster from strong optical emission lines

Zeleke Beyoro-Amado,[1,2,3★] Miguel Sánchez-Portal,[4,5★] Ángel Bongiovanni,[4,5] Mirjana Pović,[1,6★] Solomon B. Tessema,[1] Ricardo Pérez-Martínez,[5,7] Ana María Pérez García,[5,8] Miguel Cerviño,[8] Jakub Nadolny,[9,10] Jordi Cepa,[9,10] J. Ignacio González-Serrano[11] and Irene Pintos-Castro[12]

[1]*Ethiopian Space Science and Technology Institute (ESSTI), Entoto Observatory and Research Centre (EORC), Astronomy and Astrophysics Research and Development Division, PO Box 33679 Addis Ababa, Ethiopia*
[2]*Kotebe Metropolitan University (KMU), College of Natural and Computational Sciences, Department of Physics, PO Box 31248 Addis Ababa, Ethiopia*
[3]*Addis Ababa University (AAU), PO Box 1176 Addis Ababa, Ethiopia*
[4]*Instituto de Radioastronomía Milimétrica (IRAM), Av. Divina Pastora 7, Núcleo Central, E-18012 Granada, Spain*
[5]*Asociación Astrofísica para la Promoción de la Investigación, Instrumentación y su Desarrollo, ASPID, E-38205 La Laguna, Tenerife, Spain*
[6]*Instituto de Astrofísica de Andalucía (IAA-CSIC), Glorieta de la Astronomia s/n, E-18008 Granada, Spain*
[7]*ISDEFE for ESA. Camino Bajo del Castillo s/n. Urb. Villafranca del Castillo, E-28692 Villanueva de la Cañada, Spain*
[8]*Centro de Astrobiología (CSIC/INTA), ESAC Campus, Camino Bajo del Castillo s/n, E-28692 Villanueva de la Cañada, Spain*
[9]*Instituto de Astrofísica de Canarias (IAC), E-38200 La Laguna, Tenerife, Spain*
[10]*Departamento de Astrofísica, Universidad de La Laguna (ULL), E-38205 La Laguna, Tenerife, Spain*
[11]*Instituto de Física de Cantabria (CSIC - Universidad de Cantabria), Avda. de los Castros s/n, E-39005 Santander, Spain*
[12]*Department of Astronomy and Astrophysics, University of Toronto, 50 St. George Street, Toronto, ON M5S 3H4, Canada*

Accepted 2020 0. Received 2020 November 26; in original form 2020 July 23

ABSTRACT

Although ZwCl0024+1652 galaxy cluster at $z \sim 0.4$ has been thoroughly analysed, it lacks a comprehensive study of star formation and nuclear activity of its members. With GaLAxy Cluster Evolution (GLACE) survey, a total of 174 H α emission-line galaxies (ELGs) were detected, most of them having [N II]. We reduced and analysed a set of [O III] and H β tunable filter (TF) observations within GLACE survey. Using H α priors, we identified [O III] and H β in 35 (∼20 per cent) and 59 (∼34 per cent) sources, respectively, with 21 of them having both emission lines, and 20 having in addition [N II]. Applying BPT-NII diagnostic diagram, we classified these ELGs into 40 per cent star-forming (SF), 55 per cent composites, and 5 per cent LINERs. Star formation rate (SFR) measured through extinction corrected H α fluxes increases with stellar mass (M_*), attaining its peak at $M_* \sim 10^{9.8}$ M$_\odot$. We observed that the cluster centre to ∼ 1.3 Mpc is devoid of SF galaxies and AGN. Our results suggest that the star formation efficiency declines as the local density increases in the cluster medium. Moreover, the SF and AGN fractions drop sharply towards high-density environments. We observed a strong decline in SF fraction in high M_*, confirming that star formation is highly suppressed in high-mass cluster galaxies. Finally, we determined that SFR correlates with M_* while specific SFR (sSFR) anticorrelates with M_*, both for cluster and field. This work shows the importance and strength of TF observations when studying ELGs in clusters at higher redshifts. We provide with this paper a catalogue of ELGs with H β and/or [O III] lines in ZwCl0024+1652 cluster.

Key words: methods: observational – galaxies: active – galaxies: clusters: general – galaxies: star formation.

1 INTRODUCTION

Galaxy clusters are some of the largest known gravitationally bound structures, consisting of hundreds to thousands of galaxies (e.g. Press & Schechter 1974; Trenti et al. 2012). Investigating the way galaxies form and evolve in both field and clusters gives a very important information for the concern of modern cosmology. Moreover, to understand how galaxies transform inside the clusters presents one of the main steps in disentangling the picture of galaxy formation and evolution, and the formation and evolution of the Universe at large. Some of previous works observed differences between the properties of galaxies in the field and those in clusters (e.g. Dressler, Thompson & Shectman 1985; Balogh et al. 1997; Koopmann & Kenney 1998; Cucciati et al. 2010; Chung et al. 2011; Hwang et al. 2012; Delaye et al. 2014; Allen et al. 2016; Cantale et al. 2016; Maier et al. 2016; Saracco et al. 2017; Matharu et al. 2020; Old et al. 2020; Pérez-Martínez et al. 2020; Tiley et al. 2020), although the difference seems to be more significant for star-forming than for quiescent galaxies (e.g. Allen et al. 2016; Saracco et al. 2017; Old et al. 2020; Tiley et al. 2020). Specifically, the star formation activity seems to be anticorrelated with the local density (Haines et al. 2013; Kovač et al. 2014). Considering the effect of global

★ E-mail: zbamado@gmail.com (ZBA); msanchez@iram.es (MSP); mpovic@iaa.es (MP)

© 2020 The Author(s)
Published by Oxford University Press on behalf of Royal Astronomical Society

Downloaded from https://academic.oup.com/mnras/article/501/2/2430/6031334 by guest on 12 February 2026

environment, it is observed that the fraction of blue galaxies is higher in field than in clusters up to redshift of ~ 1.2 (Muzzin et al. 2012). Concerning the variations with local density, the fractions of SF and blue galaxies seem to decline as the local density increases, in low- to intermediate-redshift clusters (e.g. Kodama et al. 2004; Baldry et al. 2006; Cooper et al. 2008; Cucciati et al. 2017). On the other hand, there are studies showing correlation of the rate of quenching and the fraction of quiescent galaxies in relation to the stellar mass and local environment (e.g. Baldry et al. 2006; Vulcani et al. 2010; Kovač et al. 2014; Darvish et al. 2017; Nantais et al. 2017). Moreover, a well established relation called morphology–density relation is in place (Dressler 1980), showing that the fraction of early-type (ET) galaxies increases with local density while the fraction of late-type (LT) galaxies decreases.

Moreover, significant evolution in the properties of galaxies in clusters have been observed as a function of redshift as well as environment (e.g. Coia et al. 2005; Geach et al. 2006; Moran et al. 2007; Haines et al. 2009; Altieri et al. 2010; Koyama et al. 2011; Martini et al. 2013; Pintos-Castro et al. 2013; Sánchez-Portal et al. 2015; Pintos-Castro et al. 2016). The study of AGN population, star formation (SF) activity, morphology, colour–magnitude relations, and distribution of galaxy metallicities with cluster properties (e.g. cluster radii and local density) present the powerful mean to investigate evolution within clusters. Concerning morphology being one of the important galaxy properties, the cores of nearby clusters are dominated by red ET galaxies, while at higher redshifts the population of blue-dominated LT galaxies increases (e.g. Butcher & Oemler 1984; Bower et al. 1998; Pintos-Castro et al. 2016), the so-called BO effect. In Beyoro-Amado et al. (2019), we performed the morphological classification of galaxies in ZwCl 0024 + 1652 cluster (applying the same method as in Pović et al. 2012, 2013, 2015; Pintos-Castro et al. 2016) using *HST*/ACS data confirming that the core of this cluster is dominated by ET galaxies over the LT ones. Regarding SF activity, the increase of the obscured SF was observed in mid and far-infrared (IR) surveys of distant clusters (e.g. Coia et al. 2005; Geach et al. 2006; Haines et al. 2009).

Different results have been reported regarding AGN activity in clusters. However, the way how the AGN fraction varies with environment, and the role of AGN in galaxy transformations and evolution in galaxy clusters is still not clear. Some studies suggest that AGN activity increases with redshift (e.g. Martini et al. 2002; Eastman et al. 2007; Sivakoff et al. 2008; Martini et al. 2013) as revealed using X-ray data. There are studies that suggest that AGN fraction does not depend on the local density at all (e.g. Miller et al. 2003; von der Linden et al. 2010; Pimbblet et al. 2013; Pintos-Castro et al. 2016; Marziani et al. 2017) whereas others argue that high density regions and luminous AGNs look disjoint (e.g. Kauffmann et al. 2004; Alonso et al. 2007; Argudo-Fernández, Lacerna & Duarte Puertas 2018; Bornancini & García 2020).

Following the hierarchical model of structure formation galaxies merge into larger systems with time. This process is likely responsible for the evolution of the proprieties of cluster galaxies, as a function of redshift and environment (e.g. Balogh et al. 2000; Kodama & Bower 2001). Different physical processes like mergers and harassment (both resulting from galaxy–galaxy low- and high-speed interactions, respectively), starvation (slow decrease in SF), ram-pressure stripping, thermal interstellar mass evaporation, turbulent stripping, etc. were suggested for affecting the galaxy evolution in clusters (e.g. Gunn & Gott 1972; Larson, Tinsley & Caldwell 1980; Moore et al. 1996; Cole et al. 2000; Nipoti et al. 2007; von der Bosch et al. 2008; Roediger 2009; Dressler et al. 2013; Džudžar et al. 2019; Coccato et al. 2020). These processes may result from galaxy–intercluster medium (ICM) interactions, tidal triggering SF, or tidal halo stripping, depending on the distance from the cluster core (Treu et al. 2003). These physical processes act on the emission line galaxies (ELG) population (both SF and AGN) of the cluster (e.g. Poggianti et al. 2017). Apart from these intracluster physical processes, (e.g. Sobral et al. 2015) suggest that rapid and significant star formation and AGN activity could be addressed to massive cluster merging. In identifying the cluster ELGs, narrow-band imaging surveys have shown to be very efficient (Koyama et al. 2010; Sánchez-Portal et al. 2015). The central regions of clusters are devoid of ELGs (SF and AGN) such as H α and mid-IR emitters, and the SFRs of clusters decrease rapidly since $z \sim 1$ (e.g. Koyama et al. 2010; Koulouridis & Bartalucci 2019).

GaLAxy Cluster Evolution (GLACE) survey has been designed by taking advantage of the power of narrow-band imaging. It is an innovative survey of ELGs and aims in studying SF and AGN activity, morphology, and metallicity variations of galaxies in clusters at different redshifts (Pintos-Castro et al. 2013; Sánchez-Portal et al. 2015; Pintos-Castro et al. 2016; Beyoro-Amado et al. 2019). The sample of clusters at three redshifts ($z \sim 0.40$, 0.63, and 0.86) have been selected. The mapping of the strongest optical emission lines such as H β, H α, [N II]6583, [O II]3727, and [O III]5007 have been carried out in the selected spectra windows scanned by the TF observation. These spectral windows were chosen to be relatively free from the strong OH emission lines (Rousselot et al. 2000).

In this paper, we use the GLACE narrow band tunable filter (TF) imaging data of an intermediate redshift cluster ZwCl0024+1652 at $z = 0.395$. This cluster exhibit the so-called BO effect (Butcher & Oemler 1984). The core of the cluster is dominated by red ET galaxies (e.g. Beyoro-Amado et al. 2019, and references therein), with slightly increasing LT galaxies outwards. Moreover, Czoske et al. (2001, 2002) identified substructures in foreground and background with wide-field spectroscopic analysis. They found bimodal redshift distribution which suggests that the cluster is composed of two systems colliding (merging) along the line of sight. Even though the cluster and its member galaxies have been analysed thoroughly by different authors (e.g. Kneib et al. 2003; Treu et al. 2003; Moran et al. 2007; Geach et al. 2009; Natarajan et al. 2009; Sánchez-Portal et al. 2015; Beyoro-Amado et al. 2019), it still lacks a comprehensive study of SF and AGN properties of its member galaxies. In this work we focus on analysing the [O III] and H β emission lines for improving our knowledge on SF and AGN activity obtained through previous analysis of H α and [N II] emission lines (Sánchez-Portal et al. 2015).

The paper is organized as follows: Section 2 describes [O III] and H β TF data used in this work; in Section 3, general data reduction has been described. Determination of the list of emission lines in [O III] and H β has been done in Section 4. We present the results and analysis in Section 5. We discussed our results in Section 6 and finally, conclusions are summarized in Section 7.

The following cosmological parameters are assumed throughout this paper: $\Omega_M = 0.3$, $\Omega_\Lambda = 0.7$, $\Omega_k = 0$, and $H_0 = 70\,\mathrm{Km\,s^{-1}\,Mpc^{-1}}$. All magnitudes are given in AB system as described by Oke & Gunn (1983), unless otherwise stated.

2 DATA

ZwCl0024+1652 is a rich galaxy cluster at redshift $z = 0.395$, notable due to evidence of a possible dark matter ring around the cluster core (Jee et al. 2007). Kodama et al. (2004) have identified 2385 cluster members by computing the photometric redshift of galaxies brighter than $z' = 22.7$ over a total area of 712.79 arcmin^2. The brightest cluster galaxy (BCG) has r-band magnitude of ~ 17.74

Downloaded from https://academic.oup.com/mnras/article/501/2/2430/6031334 by guest on 12 February 2026

(Wen & Han 2013). As determined by Kneib et al. (2003) with lensing analysis, the cluster viral radius is $R_{200} = 1.7$ Mpc with a total mass of $\sim 5.7 \times 10^{14}$ M$_\odot$. The cluster was determined to be characterized by at least two dynamical structures as described in Section 5. As reported by Sánchez-Portal et al. (2015) using the GLACE data, the Hα luminosity function is well aligned with estimates from Kodama et al. (2004). In the following, we describe the data used in this work for carrying out the further studies of ZwCl0024+1652 cluster.

2.1 The GLACE TF data

Two pointings have been carried out with OSIRIS/GTC using the red TF towards Zwcl0024+1652 targeting the [O III] and Hβ lines. The first pointing (centred at RA = $00^h\,26^m\,35.70^s$, DEC = $17^d\,09^m\,45.0^s$) referred as 'centre position' or 'position A' was executed in GTC semesters 8-10AGOS, 75-13B, and 63-09B. In the centre position observations the core of the cluster was centred within CCD1.[1] The second pointing observations (centred at RA = $00^h\,26^m\,26.5^s$, DEC = $17^d\,12^m\,15.0^s$) referred as 'offset position' or 'position B' were performed in GTC semesters 75-13B and 47-10B. The position B offsets are ΔRA = -2.3 arcmin, ΔDEC = $+2.5$ arcmin; i.e. about 3.4 arcmin in the NW direction.

The [O III] line observations spanned at the spectral range of 6894.8 – 7154.8 Å that was covered by 27 evenly spaced scan steps of $\Delta\lambda = 10$ Å. Hence, there are 27 individual image slices for each position (centre position and offset position) corresponding to each wavelength. In GTC semesters 8-10AGOS and 47-10B, three individual exposures have been carried out for each TF tune with a 'L-shaped' dithering pattern with an amplitude of 10 arcsec (similar to the gap between the detectors), implemented to easily identify the diametric ghosts (see Jones, Shopbell & Bland-Hawthorn (2002) for a detailed description), while in GTC semester 75-13B, only two individual dithered exposures for each TF tune have been mapped for the same wavelength steps. The observational data of [O III] imaging is summarized in Table 1.

The spectral range of the Hβ observations was 6701.1 –6911.1 Å. For this line, the target was covered by 22 evenly spaced scan steps of $\Delta\lambda = 10$ Å at the centre position; at the offset position, two scan steps at 6901.1 Å and 6911.1 Å were omitted accidentally, hence we only have 20 image slices for position B. As in the previous case, three individual dithered exposures with a 'L-shaped' pattern were obtained for each TF tune. The Hβ imaging data are summarized in Table 2.

2.2 Ancillary cluster data

In addition to the GLACE data, we used a public master catalogue[2] data for ZwCl0024+1652 cluster described in Treu et al. (2003) and Moran et al. (2005) consisting of 73 318 sources covering the area of 0.5×0.5 deg^2 up to the cluster-centric distance of ~ 5 Mpc. This catalogue provides the morphological classification of sources brighter than $I = 22.5$ (Moran et al. 2005) and photometric data used in our analysis. The morphological classification was performed visually where spiral, lenticular, or elliptical morphologies are assigned if clearly resolved. Moreover, for the visual inspection of thumbnails we used the *HST*/ACS[3] high resolution reduced scientific images observed using the ACS Wide Field Camera (WFC) having a pixel scale of 0.05 arcsec per pixel and field of view of 202×202 arcsec^2. We also used morphological classification of galaxies from Beyoro-Amado et al. (2019). In this work authors used galaxy Support Vector Machine (galSVM; Huertas-Company et al. 2008) to classify cluster member galaxies up to a cluster-centric distance of 1 Mpc.

2.3 Galaxy data for cluster-field comparison

In order to compare selected properties of field galaxies with the cluster parameters described in this work, we explored different observed spectroscopic data sets which match the flux depth and redshift domains explored by GLACE survey, in particular the surveyed one of ZwCl0024+1652 at $z = 0.395$. We found that the VIMOS-VLT Deep Survey (VVDS-Deep; Le Févre et al. 2013) data sample in the field 0226-04 (0.61 deg^2) meets this purpose. This publicly available data base[4] contains reduced fluxes and equivalent widths (EW) of strong lines in the optical, as well as SFR and M_* estimations of 11 486 sources limited to $17.5 \leq I_{AB} \leq 24$. A detailed description of these measurements can be found in Lamareille et al. (2009). According to these authors, VVDS-Deep data has a mass-to-light completeness of 50 per cent at $z \sim 0.4$ and $\log(M_*/M_\odot) \geq 8.5$. With this mass constraint, we prepared a representative field galaxy sample by selecting from VVDS-Deep data all sources within a redshift range ($0.37 \leq z \leq 0.42$) with a continuum flux ($R_{AB} < 23$), according to the cluster galaxy distributions given by Sánchez-Portal et al. (2015). A total of 177 galaxies satisfy these criteria, increasing the final completeness of the sample to about 90 per cent.

3 DATA REDUCTION AND CALIBRATION

We carried out the basic data reduction using a TF data reduction (`TFReD`) package developed by Jones et al. (2002) and modified by GLACE members to fit OSIRIS data (Sánchez-Portal et al. 2015; Ramón-Pérez et al. 2019a, b; Bongiovanni et al. 2019, 2020). In addition, the `IDL` and `PYTHON` scripts tailored for our specific data sets, and `IRAF`[5] have been used.

For basic steps of data reduction related with bias, flat-field, and cosmic rays rejection standard `IRAF` procedures have been followed. We started the tunable filter data reduction procedures by removing the sky rings resulting from a radially changing wavelength shift as described by Gonzalez et al. (2014), following the other steps of `TFReD` data reduction as has been done in Sánchez-Portal et al. (2015). Sky ring corrected images have been prepared for source detection, as can be seen in Fig. 1.

The TF tomography technique in GLACE comprises of scans carried out with dithering described by Lara-López et al. (2010). Hence we performed combinations with median filter (Sánchez-Portal et al. 2015) and created a final deep image in each case ([O III] and Hβ) considering the dithering. We extracted the sources from each deep image with `SExtractor` (Bertin & Arnouts 1996).

[1]The mosaic of OSIRIS detector is composed of two 2048×4096 pixel CCDs separated, with a plate scale of 0.125 arcsec pixel^{-1}. Refer to Cepa et al. (2005) as well as the OSIRIS Users' manual at `http://www.gtc.iac.es/instruments/osiris/media`.

[2]http://www.astro.caltech.edu/~smm/clusters/

[3]Based on observations made with the NASA/ESA *HST*, and obtained from the Hubble Legacy Archive, which is a collaboration between the Space Telescope Science Institute (STScI/NASA), the Space Telescope European Coordinating Facility (ST-ECF/ESA) and the Canadian Astronomy Data centre (CADC/NRC/CSA)

[4]`http://cesam.lam.fr/vvds`

[5]`http://ast.noao.edu/data/software`

Downloaded from https://academic.oup.com/mnras/article/501/2/2430/6031334 by guest on 12 February 2026

Table 1. ZwCl0024+1652 imaging data targeting [O III] lines.

$\lambda_{0,\,i}$ (Å)	OS filter	Date	Seeing (arcmin)	*N*-Steps	*N*-Exp.	Exp-time (s)
Centre position: [RA = $00^h\,26^m\,35.70^s$, DEC = $17^d\,09^m\,45.0^s$]						
6894.8	f680/43	2010 July 28	0.9–1.3	4	3	45
6934.8	f694/44	2010 July 28	1.0–1.3	14	3	45
7074.8	f709/45	2010 July 28	0.9–1.3	9	3	45
6894.8	f680/43	2013 October 9	< 1.0	4	2	53
6934.8	f694/44	2013 October 9	< 1.0	14	2	53
7074.8	f709/45	2013 October 9	< 1.0	9	2	53
Offset position: [RA = $00^h\,26^m\,26.5^s$, DEC = $17^d\,12^m\,15.0^s$]						
6894.8	f680/43	2010 September 20	0.9–1.3	4	3	45
6934.8	f694/44	2010 September 20	1.0–1.3	14	3	45
7074.8	f709/45	2010 September 20	0.9–1.3	9	3	45
6894.8	f680/43	2013 October 9	< 1.0	4	2	53
6934.8	f694/44	2013 October 9	< 1.0	14	2	53
7074.8	f709/45	2013 October 9	< 1.0	9	2	53

Table 2. ZwCl0024+1652 imaging data targeting H β lines.

$\lambda_{0,\,i}$ (Å)	OS filter	Date	Seeing (arcmin)	*N*-Steps	*N*-Exp.	Exp-time (s)
Centre position: [RA = $00^h\,26^m\,35.70^s$, DEC = $17^d\,09^m\,45.0^s$]						
6701.1	f666/36	2009 November 24	0.8–1.0	5	3	124
6751.1	f666/36	2009 November 25	1.1–1.2	3	3	124
6781.1	f680/43	2009 November 25	0.8–1.0	2	3	124
6801.1	f680/43	2010 August 17	1.0	3	3	130
6831.1	f680/43	2009 November 24	0.9– 1.1	5	3	124
6881.1	f680/43	2009 November 24	0.8–1.0	4	3	124
Offset position: [RA = $00^h\,26^m\,26.5^s$, DEC = $17^d\,12^m\,15.0^s$]						
6701.1	f666/36	2013 October 9	< 1.0	5	3	138
6751.1	f666/36	2013 October 9	< 1.0	3	3	138
6781.1	f680/43	2013 October 9	< 1.0	2	3	138
6801.1	f680/43	2013 October 9	< 1.0	5	3	138
6851.1	f680/43	2013 October 9	< 1.0	5	3	138

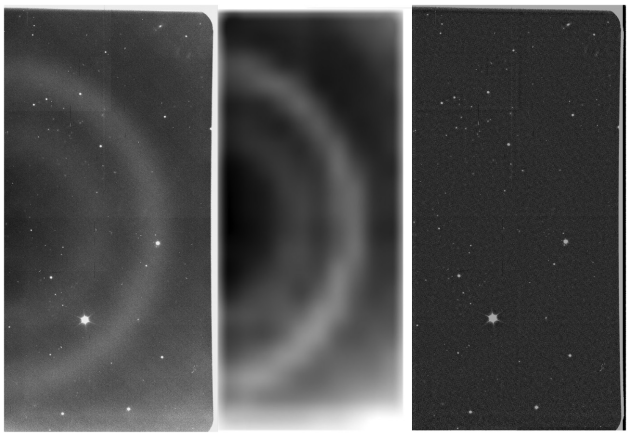


Figure 1. Example of image of H β obtained for removing the sky rings using `TFReD` package. This is a CCD2 image obtained with the TF tuned at 6881.1 Å before subtraction of the sky rings (left-hand panel), the background sky map created by the `tringSub2` task (centre), and the same image after the subtraction of the sky rings (right-hand panel).

Considering two images (image1 and image2) with the same central wavelength (λ) in two different dithering positions, the wavelength difference for a particular source (at respective distances of r_1 and r_2 in arcsec to the optical centre) was estimated as:

$$\Delta\lambda = \lambda_1 - \lambda_2 = 5.04(r_2{}^2 - r_1{}^2) + (6.0396 - 1.5698 \times 10^{-3}\lambda + 1.0024 \times 10^{-7}\lambda^2) \times (r_1{}^3 - r_2{}^3). \quad (1)$$

For tuned wavelength and each detected source we determined the best possible combination and derived the equivalent transmission profile. This resulted with centre/offset possible combinations of 1301/1162 and 325/298 in the case of [O III] and H β, respectively. We selected a catalogue of 266 sources from *GAIA* (Lindegren et al. 2016, 2018) covering the entire field with sky positions of reference objects for mapping the cluster by performing astrometry and then determined the astrometric solution with standard `IRAF` tasks `ccxymatch` and `ccmap`. To measure the flux at each slice and source position, we generated set of degraded images using `TFReD` specific task; `tfwhm` (for measuring the FWHM) and `tgauss`. For more detailed description see Sánchez-Portal et al. (2015).

Having a catalogue from deep image and performing photometry on the degraded images, we generated a raw catalogue of candidates by using `tsex` and `tespect` routines of `TFReD`. We separated

Downloaded from https://academic.oup.com/mnras/article/501/2/2430/6031334 by guest on 12 February 2026

Table 3. Spectrophotometric standard stars; the top three for centre while the bottom two for offset position observations.

Name	Mag (λ, Å)	Reference
G158-100	14.87 (5400)	Filippenko & Greenstein (1984)
L1363-3	13.28 (5560)	Oke (1974)
Feige 110	11.82 (5556)	Massey & Gronwall (1990)
G191-B2B	11.72 (5460)	Oke (1990)
G157-34	15.35 (5400)	Filippenko & Greenstein (1984)

the non-star-like form from star-like sources and produced flux and flux-error files, containing a non-calibrated pseudo-spectra and a corresponding error in flux, respectively. For [O III] and H β centre/offset position we detected a total of 724/1168 and 945/1277 non-star-like candidates, respectively. A pseudo-spectrum is a file consisting of tuples with wavelength (λ) at source position and flux value. It differs from a standard spectrum produced by dispersive medium in that it's flux at each point results from integrating within a passband of the filter centred at the point's wavelength as depicted in Sánchez-Portal et al. (2015).

For wavelength calibration we first determined the optical centre and the effective wavelength of the observation for each image. Based on Sánchez-Portal et al. (2015), we considered the solution to converge for consecutive wavelength difference lower than 1 Å. We followed a two-step procedure in performing the flux calibration of each TF tune. The first step is to derive the total efficiency $\epsilon(\lambda)$ of the system (telescope, optics, and detector) using a flux measured with aperture photometry and a published flux at given wavelength for set of exposures of the spectrophotometric standard stars (Table 3).

The final step in flux calibration is converting the extracted flux to physical units. For each source at each single *i*-th exposure, having the total efficiency $\epsilon(\lambda)$ already estimated, we converted the measured flux $f_{\rm ADU}(\lambda)_i$ to actual flux $f_{\rm m}(\lambda)_{\rm i}$ in erg s^{-1} cm^{-2} Å^{-1} by using:

$$f_m(\lambda)_{\rm i} = f_{\rm ADU}(\lambda)_{\rm i} \frac{g\,K(\lambda)\,E_\gamma(\lambda)}{\epsilon(\lambda)\,t\,A_{\rm tel}\,\delta\lambda_{\rm e}}, \quad (2)$$

where g denotes the CCD gain in e^{-1} ADU^{-1}, $E_\gamma(\lambda)$ stands for the energy of photon in erg, t is the exposure time in seconds, $A_{\rm tel}$ is the area of the primary mirror of the telescope in cm^2, $\delta\lambda_{\rm e}$ is the effective passband width in Å, while $K(\lambda)$ stands for atmospheric extinction correction. More detailed information on data reduction and calibration can be found in in Sánchez-Portal et al. (2015).

4 THE [O III] AND H β EMITTERS

4.1 Identifying the emission line candidates through H α priors

We cross-matched [O III] non-star-like catalogues of 724/1168 centre/offset sources with the catalogue of ELGs confirmed through H α priors (Sánchez-Portal et al. 2015) using a radius of 1 arcsec and found 114 and 95 counterparts for centre and offset positions, respectively, with 57 common sources. In Sánchez-Portal et al. (2015), 174 H α emitters with derived redshifts were confirmed after removing contaminants (Kodama et al. 2004). The redshifts are distributed in $0.35 \leq z \leq 0.45$ range and were checked to be consistent by comparing with spectroscopic redshifts from Moran et al. (2005). After merging results from both positions and removing common sources, we identified a total of 152 unique ELGs as preliminary [O III] emission line candidates with H α counterparts.

Similarly, in case of H β data we obtained 945 and 1277 sources in centre and offset position, respectively. After cross-matching both catalogues with H α ELGs, we obtained 127 and 102 matches for the centre and offset positions, respectively, with 67 duplicates. Finally, we identified a total of 162 ELGs as preliminary candidates for H β line emission. For all the [O III] and H β candidates we measured their fluxes, as described in following sections.

4.2 Computation of the [O III] line fluxes

To compute [O III] fluxes we used the previous results of calibration in Section 3. We used a suited python script in determining the [O III] fluxes. With median flux value of all sources ($\widetilde{f}_{\rm all}$) and standard deviation ($\sigma_{\rm all}$), we took a pseudo-continuum from the simulated pseudo-spectra as part of pseudo-spectrum points by discarding 'high/low' values of the outliers: the sources with $f > \widetilde{f}_{\rm all} + 2 \times \sigma_{\rm all}$ ('high' outliers) or sources with $f < \widetilde{f}_{\rm all} - 2 \times \sigma_{\rm all}$ ('low' outliers). Hence, we defined the median as the continuum level ($f_{\rm cont}$) and its standard deviation ($\sigma_{\rm cont}$) to be the continuum noise (error). By finding the continuum-subtracted flux ($f_{\rm cs}$([O III])) belonging to the peak in a range of ± 2 scan steps (± 20 Å) within the predicted wavelength ($\lambda_{\rm pred}$) of the [O III] line and a TF effective transmission at the line wavelength (T([OIII])), flux is computed as

$$f([\mathrm{OIII}]) = f_{\rm cs}([\mathrm{OIII}]) \times T([\mathrm{OIII}]). \quad (3)$$

Flux error is determined with the error propagation formula as

$$\Delta f([\mathrm{OIII}]) = T([\mathrm{OIII}]) \times \sqrt{(\Delta f_{\rm b}([\mathrm{OIII}]))^2 + (\sigma_{\rm cont})^2}, \quad (4)$$

where $\Delta f_{\rm b}([OIII])$ is a flux error before continuum subtraction. We used equation (5) to compute $\lambda_{\rm pred}$ using the redshift (z) derived with H α results and the rest frame wavelength ($\lambda_0 = 5007$ Å):

$$\lambda_{\rm pred} = \lambda_0 \times (1 + z). \quad (5)$$

The python script was applied to all the 152 preliminary [O III] candidates. While fluxes have been measured for 67/50 sources in centre/offset positions respectively with 23 duplicates. Finally, after visual inspection of pseudo-spectra we remained with 51 [O III] candidates.

4.3 Derivation of H β fluxes

In case the TF collected flux is just the sum of the continuum (considerable absorption) and the H β emission line. A total H β emission is obtained by following a slightly similar process as for the [O III] case, but here involving the absorption correction. We first computed a continuum-subtracted flux ($f_{\rm cs}$(H β)) following the same procedure as for [O III].

For measuring the equivalent width (EW) of H β, we went through the spectral energy distribution (SED) fitting, using the standard templates (Bruzual & Charlot 2003, hereafter BC03) and `LePhare` code (Ilbert et al. 2006). Since `LePhare` makes use of the low-resolution composite stellar populations (CSP) while for measuring the EW(H β) we require a high-resolution SED templates, we obtained the best-fitting host galaxy stellar template re-sampled at a finer resolution using the `GALAXEV`[6] code (BC03). We derived the spectral evolution of the CSPs by integrating the equation of evolution of single stellar population (SSP) templates from BC03 with metallicities $Z = 0.0001$, 0.0004, 0.004, 0.008, and 0.02 with star formation histories exponentially varying with time as SFR $\propto e^{-t/\tau}$, where τ ranges from 0.1 to 30.0 Gyr and taking the

[6] http://www2.iap.fr/users/charlot/bc2003/

Downloaded from https://academic.oup.com/mnras/article/501/2/2430/6031334 by guest on 12 February 2026

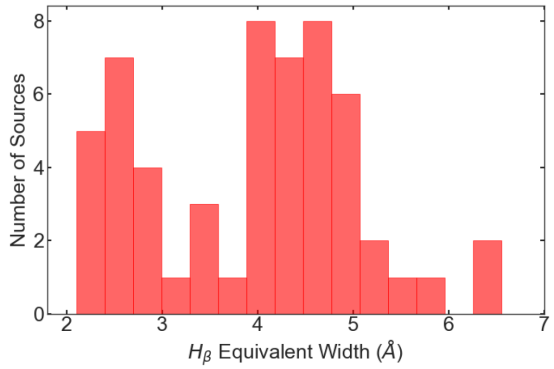


Figure 2. Distribution of H β absorption line equivalent widths derived from the best-fitting templates and ages.

initial mass function (IMF) from Chabrier (2003). The output of this code includes the EW(H β) at different ages as defined in Trager et al. (1998). Without applying the interpolation since both codes implement almost identical age steps, we have chosen the values of EW(H β) at the closest ages to those given by the best fit from `LePhare`. The distribution of EW(H β) is given in Fig. 2 for the identified H β lines, with the average ratio equivalent width being 4.0 Å.

The absorption line flux was measured by multiplying the value of EW(H β) by the previously derived pseudo-continuum. In average, the flux ratio is $f_{\mathrm{H}\beta,\mathrm{absorption}}/f_{\mathrm{H}\beta,\mathrm{emission}} \simeq 0.43$. The next step is calculating the flux in absorption given by $f_{\mathrm{abs}} = \mathrm{EW}_{\mathrm{H}_\beta} \times f_{\mathrm{cont}}$. The total flux ($f_{\mathrm{total}}$) is then finally computed as a sum of the continuum-subtracted flux ($f_{\mathrm{cs}}(\mathrm{H}\beta)$) and the flux in absorption as $f_{\mathrm{total}}(\mathrm{H}_\beta) = f_{\mathrm{cs}}(\mathrm{H}\beta) + f_{\mathrm{abs}}$, and we determined the final line flux errors using the error propagation formula (now including absorption), including error in absorption as

$$\Delta f_{\mathrm{total}}(\mathrm{H}\beta) = \sqrt{(\Delta \mathrm{f}(\mathrm{H}\beta))^2 + (\sigma_{\mathrm{cont}} \times \mathrm{EW}(\mathrm{H}\beta))^2}. \quad (6)$$

We obtained flux measurements for 69 and 75 sources in central and offset positions, respectively, with 28 duplicates. After the visual inspection of pseudo-spectra, we identified 80 final candidates for H β emission.

4.4 Analysis of individual objects and selection of the final sample of [O III] and H β emitters

We obtained in total 51 [O III] and 80 H β emission line final candidates with 29 common candidates for both lines resulting with a total of 102 unique candidates, as described in Sections 4.2 and 4.3. For final sample selection and to make sure that fluxes are coming from single sources, we first went through the visual inspection of thumbnails from *HST* data described in Section 2.2. In total, we found thumbnails of 31 and 52 [O III] and H β candidates, respectively, with 19 sources in common. Most of the sources ($\sim$91 per cent) were inspected to be well isolated. Secondly, for remaining sources we inspected the H α pseudo-spectra (Sánchez-Portal et al. 2015), and removed those sources with line offset of $\geq$10 Å and/or those sources with no clearly detected peak. We finally detected all targeted emission lines ([O III], H β, [N II], and H α) for 20 ELGs. Our final sample is summarized in Table 4. Fig. 3 gives an example of sources with [O III] and/or H β lines, showing the ACS thumbnails and available pseudo-spectra.

Table 4. The number of preliminary candidates for [O III] and/or H β emission; with final detected emission line sources.

Sources	[O III]	H β	[O III] and H β	[O III] + H β + [N II] + H α
Pre-candidates	51	80	29	28
Final emitters	35	59	21	20

5 ANALYSIS AND RESULTS

5.1 Redshift, flux, and luminosity distributions of [O III] and H β line emitters

Redshifts of nearly spectroscopic-quality were derived in Sánchez-Portal et al. (2015) from the positions of the H α emission lines for all our ELGs. We computed the redshifts through detected [O III] and H β lines and then compared our results with H α redshifts presented in Sánchez-Portal et al. (2015). In Fig. 4 we show the distribution of redshifts as compared with H α measurements. The relative redshift deviations, defined as $|z_{\mathrm{TF}} - z_{\mathrm{H}\alpha}|/(1 + z_{\mathrm{H}\alpha})$, are $\sim$0.002 and $\sim$0.001 for [O III] and H β, respectively, confirming therefore the spectroscopic quality of the TF-derived redshifts. Our redshift distributions are in line with previous results (Czoske et al. 2002; Sánchez-Portal et al. 2015), with average redshifts of $\sim$0.392 and $\sim$0.394 for [O III] and H β lines, respectively. Moreover, we recover two dynamical structures represented by double-peaks in the redshift distribution, where structure 'A' (centred at $z \simeq 0.395$) corresponds to the main cluster, while structure 'B' (centred at $z \simeq 0.380$) represents the infalling component (Czoske et al. 2002; Kneib et al. 2003; Moran et al. 2007; Sánchez-Portal et al. 2015). Our redshift measurements are also in good agreement with those obtained from H α data (Sánchez-Portal et al. 2015), as can be seen in Fig. 4 (middle and bottom plots), with linear correlation factors of 0.923 and 0.941, respectively. As determined by Czoske et al. (2002), the velocity distribution of structure A was determined to be regular with a dispersion of $\sim$600 km s^{-1} at projected distance >3 arcmin, while the formal velocity dispersion within 5 arcmin is $\sigma_{\mathrm{cent}} = 1050$ km s^{-1} for 193 galaxies. The environment conditions were parametrized by the local surface density computed by Pérez-Martínez et al. (in preparation) from the distance to the 5th-neighbour (Σ_5), according to Dressler et al. (1985). Moreover, we computed the radial velocity of each member galaxy and derived the projected cluster-centric distance separately for H β and [O III] emitters to produce and discuss on the projected phase–space diagrams shown in Fig. 5.

The statistics of the distributions of fluxes and luminosities of [O III] and H β are given in Tables 5 and 6. A comparison of these distributions with those of H α and [N II] is depicted in Fig. 6. We found that [O III] and H β fluxes and luminosities are on average comparable with H α and [N II] values, although slightly lower. As a further comparison, median fluxes of H α and [N II] are 1.9×10^{-16} and 7.7×10^{-17} erg s^{-1} cm^{-2}, respectively. Median logarithmic luminosities (log L) are 41.0 and 40.6 erg s^{-1}, respectively.

5.2 Morphologies of the [O III] and H β emitters

In this work we used morphological classification from Beyoro-Amado et al. (2019). Moreover, Treu et al. (2003) and Moran et al. (2007) have previously carried out a visual classification

Downloaded from https://academic.oup.com/mnras/article/501/2/2430/6031334 by guest on 12 February 2026

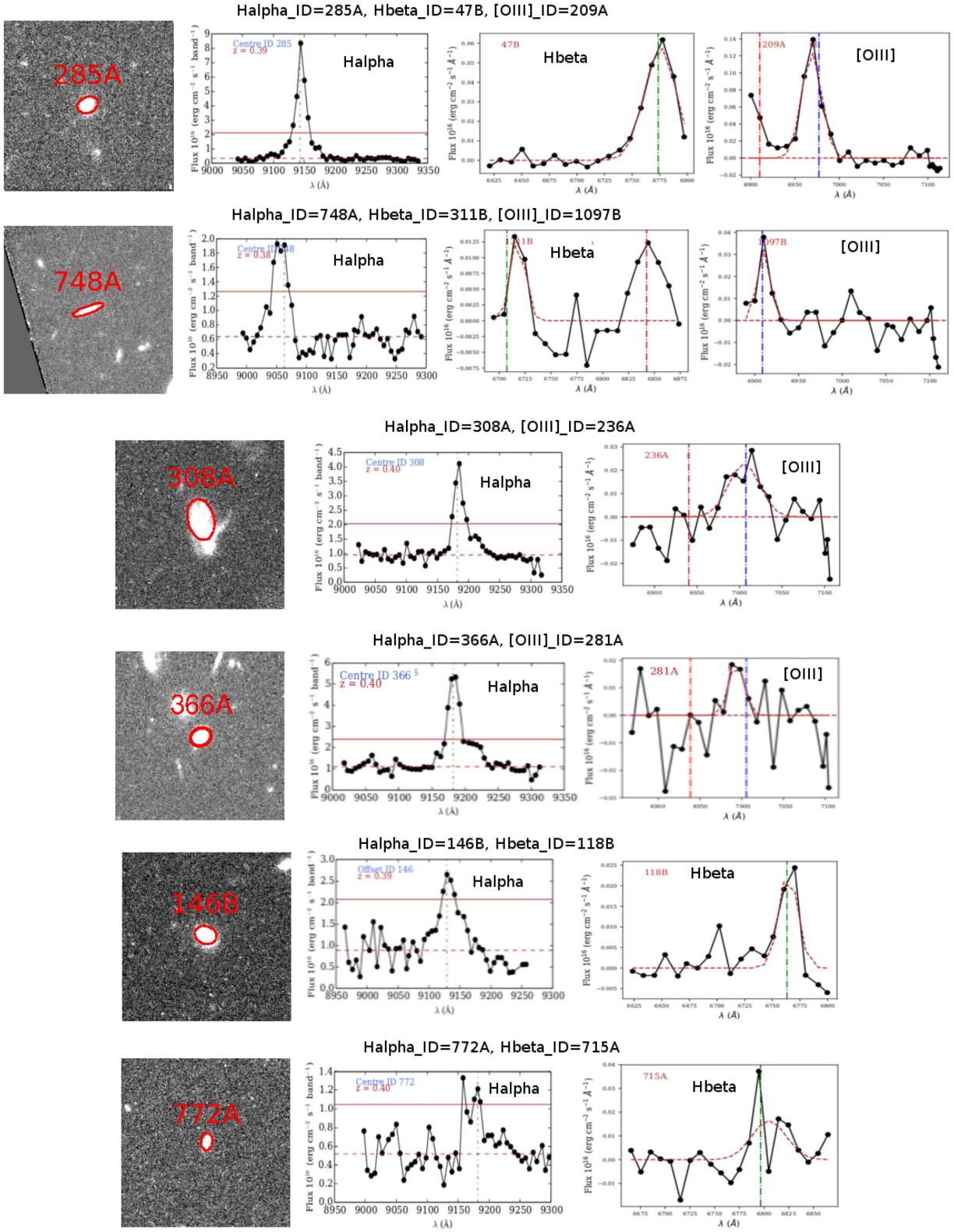


Figure 3. Example of *HST*/ACS thumbnails (left-hand panel) and pseudo-spectra of ELGs with Hα (second column), and [O III] and/or Hβ emissions (third and/or fourth columns, as indicated on each pseudo-spectrum). The predicted Hα position with spectroscopic redshifts (Moran et al. 2007) and the predicted Hβ line wavelength positions derived with Hα redshifts are represented with green vertical lines in their corresponding pseudo-spectra, while the predicted wavelength positions for [O III]5007 and [O III]4959 both computed with Hα are indicated with blue and red vertical lines, respectively, when detected.

Downloaded from https://academic.oup.com/mnras/article/501/2/2430/6031334 by guest on 12 February 2026

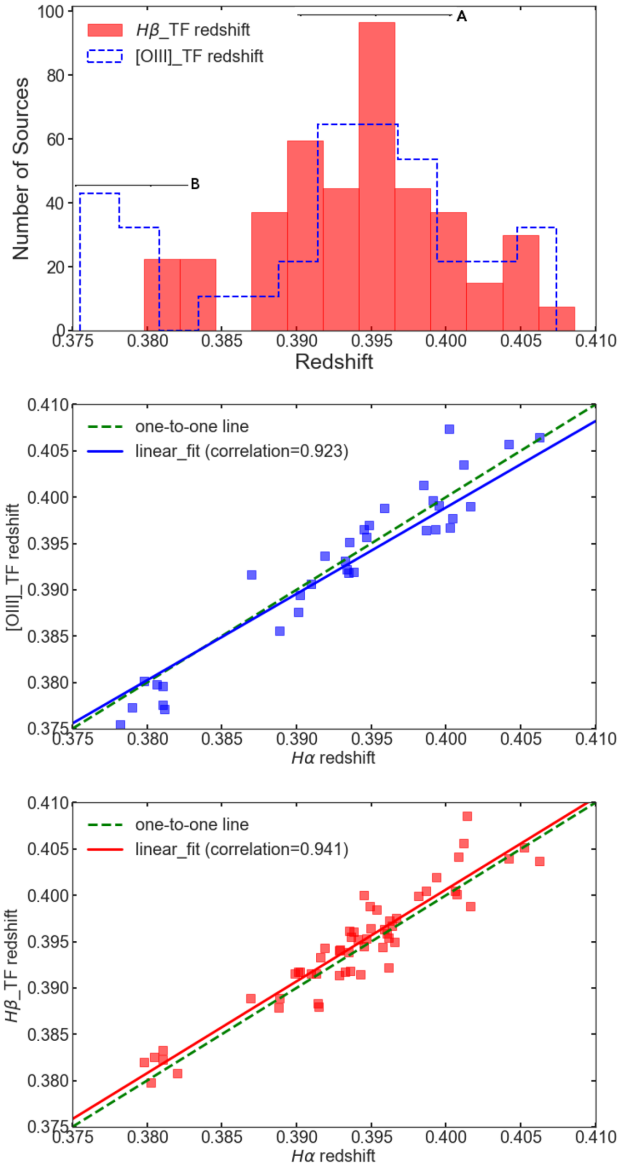


Figure 4. Redshift distribution of [O III] and H β ELGs (top plot). Two dynamical structures A and B can be seen, as suggested in previous works (Czoske et al. 2002; Sánchez-Portal et al. 2015). In addition, linear correlation between [O III] (middle plot) and H β (bottom plot) TF derived redshifts and H α redshifts has been represented.

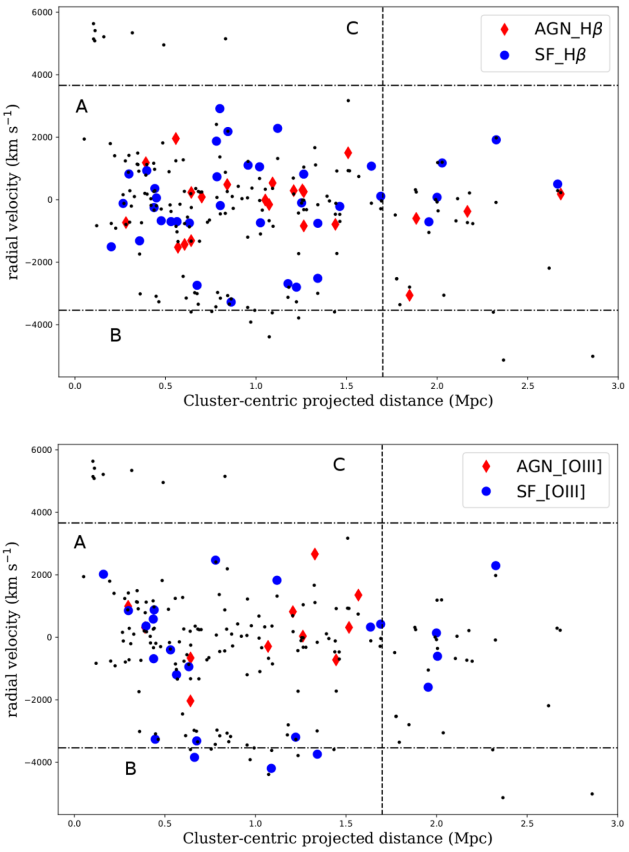


Figure 5. Radial velocity versus cluster-centric distance for H β (top plot) and [O III] (bottom plot) ELGs. The red diamonds represent AGNs while blue dots correspond to SF galaxies. The virial radius (r_{vir} = 1.7 Mpc) is represented by dotted vertical line (Treu et al. 2003). The dashed-dotted horizontal lines stand for the radial velocity limits fully covered within the field of view of the two OSIRIS TF pointings. The small black points correspond to ELGs from Sánchez-Portal et al. (2015) with H α emission. The two reported structures of the cluster are marked with 'A' and 'B', whereas the putative possible component is represented with letter 'C'.

within 5 Mpc of the cluster centre. In all these works galaxies have been classified between early-type (ET) and late-type (LT). After cross-matching our data with all the three references, we found morphological classes for 24 [O III] emitters (8 ET and 16 LT), and 41 H β sources (13 ET and 28 LT), leaving significant number of sources without classification. This could be because Beyoro-Amado et al. (2019) classification is only within 1 Mpc and others give classification only for brightest sources. This gives us similar fractions of ETs (33 per cent for [O III] and 32 per cent in case of H β), and LTs (67 per cent for [O III] and 68 per cent for H β).

As expected, we found a larger populations of LT galaxies, and on average their [O III] and H β emission lines are similar to those of ETs. Median logarithmic luminosities (log L) of LT and ET are 40.59

Table 5. The statistical distribution of fluxes of [O III] and H β emitters in erg s^{-1} cm^{-2}; with Q_1 being first quarter, Q_3 being third quarter, and Med representing median.

Emission line	Q_1	Med	Q_3	Adopted flux limit
[OIII]	3.7×10^{-17}	6.2×10^{-17}	1.0×10^{-16}	2.5×10^{-17}
H β	4.1×10^{-17}	1.3×10^{-16}	7.4×10^{-17}	2.0×10^{-17}

Table 6. The statistical distribution of logarithm luminosities (Q_1, Med, Q_3) in erg s^{-1} of [O III] and H β emitters.

Emission line	Q_1	Med	Q_3
[OIII]	40.3	40.5	40.7
H β	40.3	40.6	40.9

Downloaded from https://academic.oup.com/mnras/article/501/2/2430/6031334 by guest on 12 February 2026

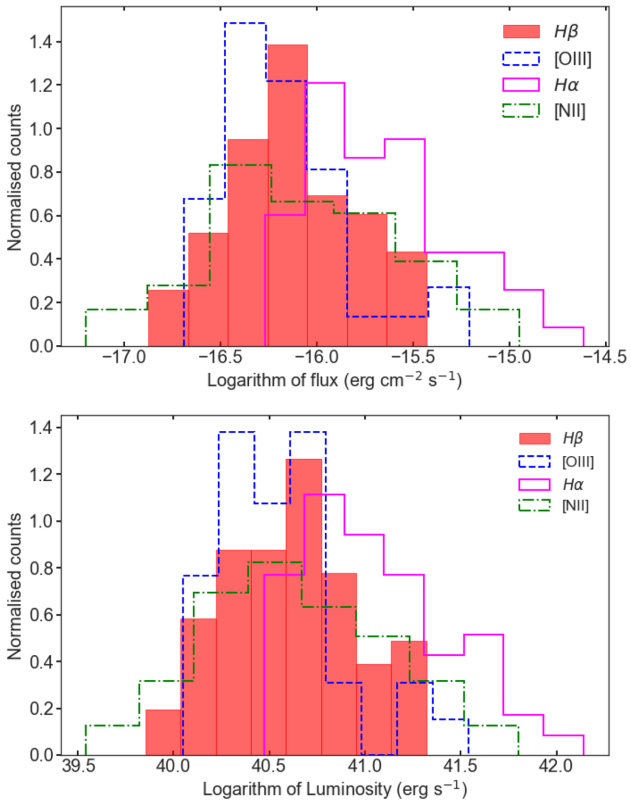


Figure 6. Comparison of the flux (top plot) and luminosity (bottom plot) of H β (red filled histogram), [O III] (blue dashed line), H α (violet solid line), and [N II] (green dash-dotted line) ELGs.

and 40.54 erg s^{-1} in the case of [O III], and 40.68 and 40.62 erg s^{-1} in the case of H β, respectively.

5.3 AGN versus SF classes: BPT diagrams

For the sources with all the four lines detected (as described in Table 4), we checked their spectral type using the BPT-NII diagnostic diagram (Baldwin et al. 1981; Kewley et al. 2006), separating galaxies into star-forming (SF), composite and AGN (Seyfert–2 or LINERs), as shown in Fig. 7. As a previous step, we segregated the 15 sources in our sample classified as broad-line AGNs (BLAGN) in Sánchez-Portal et al. (2015). We identified 9 ELGs with [O III], [N II] and H α detections and H β non-detected, as well as 28 ELGs with H β, [N II], and H α flux measurements but without detection of the [O III] line. In order to include these sources in the BPT-NII plot we used the flux limits shown in Table 5 to assign upper bounds to non-detections, which are represented with upward or downward arrows in this figure. The boundary between SF and composite galaxies was taken from Kauffmann et al. (2003), and between composite and AGNs from Kewley et al. (2001). To separate between LINERs and Seyfert–2 galaxies we used the prescription from Schawinski et al. (2007). The minimum and maximum limits (for [O III]/H β and [N II]/H α) were adapted from Kewley et al. (2006). Although all of these boundaries have been established using a sample of galaxies with redshifts $z < 0.1$, and although our cluster galaxies are at $z \sim 0.4$, we consider no significant evolution taking into account results of Kewley et al. (2013) verifying that the relation remains valid up to $z \sim 1$.

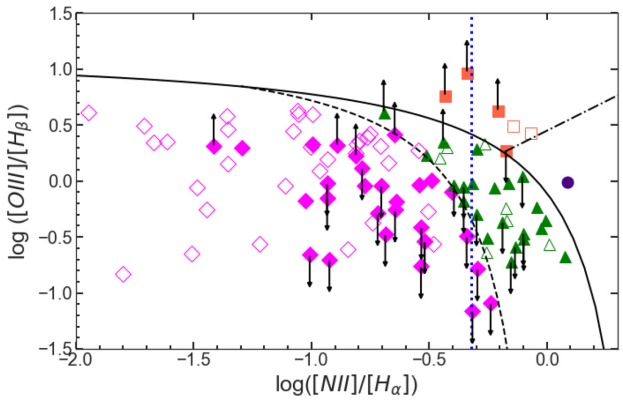


Figure 7. BPT diagram for separating SF (magenta), composite (green), Seyfert-2 (red), and AGN–LINER (indigo) ELGs. The filled symbols represent the cluster sources and the open ones the field galaxies. The arrows correspond to the cluster ELGs with either [O III]- or H β-only line detection (upward for [O III], while downward for H β). Continuous, dashed, and dot-dashed lines correspond to the boundaries given by Kewley et al. (2006), Kauffmann et al. (2003), and Schawinski et al. (2007), respectively. The vertical dotted line marks the SF-AGN separation, as prescribed by Kauffmann et al. (2003). More details are given in the text.

Table 7. Summary of our spectral classification of galaxies in ZwCl0024+1652 cluster using BPT diagram as shown in Fig. 7.

Emission	SF	Comp.	AGN(Sy2+LINER)	Total
No H β detection	4	2	3	9
No [O III] detection	17	10	1	28
All lines detected	8	11	1	20
Total	29	23	5	57

In our cluster sample, we found a total of 29 (51 per cent) SF galaxies (8 with all emission lines, 4 with no H β detection, 17 with no [O III] detection), 23 (40 per cent) composites (11 with all emission lines, 2 with no H β detection, 10 with no [O III] detection), 1 (2 per cent) LINER galaxy with all emission lines and 4 (7 per cent) Seyfert–2 ELGs (1 with no [O III] detection and 3 with no H β detection). The results of our classification are summarized in Table 7.

Additionally, we selected all the galaxies with detected emission in the chemical species cited above from the VVDS-Deep field sample described in Section 2.3. From 177 field sources we identified 41 sources having all the four lines. We segregated 32 (78 per cent) SF galaxies, 7 (17 per cent) composite, and 2 (5 per cent) Seyfert-2 galaxies, also represented in Fig. 7 (open symbols). According to this, with the caveat regarding the small-number statistics, there are $\sim$1.5 times more SF galaxies in the field and almost one-third less AGN+composite galaxies than in cluster galaxies. These differences are about three times the mean uncertainty derived from a Poissonian statistics derived from the absolute numbers of field galaxies belonging to each spectral type.

Hereafter, and in order to overcome the limitation imposed by the need of simultaneous detection of both the [O III] and H β lines, we will use the simplified criterion applied by Sánchez-Portal et al. (2015) to separate SF galaxies from AGN hosts, based on the prescription of Kauffmann et al. (2003), namely the boundary defined by the flux ratio [N II]/H $\alpha = 0.478$. With this assumption, the analysis and discussion described in the following sections is based on a segregated total of 35 SF galaxies and 22 AGN hosts.

Downloaded from https://academic.oup.com/mnras/article/501/2/2430/6031334 by guest on 12 February 2026

We compared our results here with statistics from Sánchez-Portal et al. (2015). Out of 174 ELGs in Sánchez-Portal et al. (2015), 60 (34 per cent) were AGN hosts while 114 (66 per cent) were found to be SF galaxies. Our work gave similar results with nearly comparable distribution: 38.5 per cent AGN hosts with 61.5 per cent SF galaxies. The sky distribution of H α sample including our [O III] and H β results is presented in Fig. 8. The sky positions of the ELGs is described on a blended image of an inverted RGB composed of deep images determined as in Section 3 with H α image. Finally, applying the same rule to the VVDS-Deep population, we segregated a total of 39 SF field galaxies and 7 AGN hosts. A broader discussion on comparison between cluster and field galaxies is given in Section 6.4.

5.4 Extinction-corrected star formation rate

We used the total H β flux, measured as the sum of the emission and absorption components computed as explained earlier, to compute the extinction correction from the Balmer decrement $f_{H\alpha}/f_{H\beta}$ using equation (7) below:

$$A_{\mathrm{H}\alpha} = \frac{2.5}{k_{\mathrm{H}\alpha}/k_{\mathrm{H}\beta} - 1} \log\left(\frac{1}{2.85}\frac{f_{\mathrm{H}\alpha}}{f_{\mathrm{H}\beta}}\right), \tag{7}$$

where $k_{\mathrm{H}\alpha}/k_{\mathrm{H}\beta} = 1.48$ for the galactic extinction law from Seaton (1979). The distribution of the computed extinction values is represented in Fig. 9. The largest peak corresponds to unabsorbed galaxies ($A_{\mathrm{H}\alpha} \simeq 0$). This could be expected since, due to the incompleteness of the H β sample (the H β line is actually detected for 59 galaxies ($\sim$ 34 per cent) out of 174 H α emitters), our observations favour the detection of strong H β emitters, i.e. intrinsically luminous sources or unabsorbed ones. On the other hand, a second peak close to $A_{\mathrm{H}\alpha} \simeq 0.75$ is observed, which is consistent with the usual assumption ($\sim$ 1 mag) after Kennicutt (1992).

The average uncertainty of the Balmer decrement obtained by error propagation from equation (7) is about 0.88 mag. Its relative error is 27.1/37.5 per cent (median/mean). Once we derive the extinction correction, the SFR can be computed using a suitable scaling relation, as given by Kennicutt (1998):

$$\mathrm{SFR}(M_{\odot}\mathrm{yr}^{-1}) = \frac{10^{A_{\mathrm{H}\alpha}/2.5}}{1.58} 7.94 \times 10^{-42} L(\mathrm{H}\alpha)(\mathrm{erg\ s}^{-1}), \tag{8}$$

where the factor 1.58 corresponds to the conversion from Salpeter to Chabrier (2003) initial mass function (IMF). The distributions of uncorrected and corrected H α SFR are depicted in the top panel of Fig. 10.

The errors in both the uncorrected and corrected SFR have been computed as usual by propagation. The average uncertainty in the uncorrected SFR is 19.5/20.9 per cent (median/mean). However, given the large uncertainty in $A_{\mathrm{H}\alpha}$, the fractional errors in the corrected SFR are much larger, 67.3/71.2 per cent (median/mean) in our case.

The correlation between the uncorrected and corrected SFR is depicted in the bottom panel of Fig. 10. Even though the results should be taken with caution, given the large uncertainties involved, a quite clear correlation is observed. Moreover, if the range is restricted to $\mathrm{SFR}_{\mathrm{H}\alpha,\,\mathrm{corrected}} < 12\,\mathrm{M}_{\odot}\,\mathrm{yr}^{-1}$, thus avoiding two objects that are luminous and highly absorbed ($A_{\mathrm{H}\alpha} = 2.43$ mag), a reasonable linear correlation equal to 0.91 with slope of 1.23 is observed considering all the sources including sources with $A_{\mathrm{H}\alpha} = 0$ (green dashed line in Fig. 10, bottom plot); while excluding the sources with $A_{\mathrm{H}\alpha} = 0$, the correlation factor is changed slightly to 0.89 with 1.00 being a new slope (red dashed line in Fig. 10, bottom plot). We performed a quantitative comparison between the two (uncorrected and corrected SFR) by using Kolmogorov–Smirnov two sample (KS2) test. We computed the p-value of our data to be 0.28, showing that both are coming from the same distribution.

6 DISCUSSION

6.1 Morphological and spectral classes of the cluster members with [O III] and H β emission

In Beyoro-Amado et al. (2019) it was discussed in detail that the morphological fractions of ZwCl0024+1652 member galaxies vary with cluster-centric distance in such a way that ET galaxies dominate over the LTs at least up to a cluster-centric distance of $\sim$ 1 Mpc. Other studies also suggested that the cores of nearby clusters have lower LT than the ET fraction, and that LT fraction increases with cluster-centric distance while the ET fraction decreases (e.g. Whitmore, Gilmore & Jones 1993; Fasano et al. 2012, 2015; Pintos-Castro et al. 2016; Kelkar et al. 2019). In addition to this, Oh et al. (2018) showed that beside ET galaxies, passive spirals can also be found in highly dense regions, such as cluster centres, suggesting that they have gone through environmental quenching. Our TF [O III] and H β observations result with detection of the brightest sources. As showed in Section 5.2, despite small sample our results show that LT galaxies dominate over the ETs when dealing with ELGs, as expected. In addition to this, our results are in general in line with previous ones where LT galaxies show to be in average at larger cluster-centric distances (e.g. Nantais et al. 2013; Fasano et al. 2015). We found that median cluster-centric distances of LT and ET ELGs are 1.82 and 1.60 Mpc when dealing with [O III] emitters and 1.93 and 1.61 Mpc in the case of H β emitters, respectively. We also present a phase–space relation of H β and [O III] ELGs separated with morphology in Fig. 11. Apart from small statistics, from Fig. 11 we deduce that the inner most region of the cluster (projected cluster-centric distance $\lesssim$ 0.3 Mpc) is almost devoid of ELGs with morphologies (ET as well as LT). Moreover, from Fig. 12 taking the morphological distributions in relation to radial distance, we can see that LT ELGs are more dispersed along the cluster-centric distance than ETs. In addition to the results obtained in Beyoro-Amado et al. (2019) we can now see from this work using TF [O III] and H β data that ET galaxies with signs of either AGN or SF activity seem to avoid the most central parts of ZwCl0024+1652 cluster.

Another point that we raise here is the distribution of spectral types within the cluster. Previous works showed that cores of regular galaxy clusters are characterized by high density while density decreases outwards with cluster-centric distance (e.g. Treu et al. 2003; Weinmann et al. 2006; Fasano et al. 2015). Our results presented in Fig. 12 agree with these results. When representing all ELGs that belong to the principal cluster structure, anticorrelation can be observed between Σ_5 and cluster-centric distance. This monotonic relation of local density to the cluster-centric distance indicates that our cluster is a regular one. Taking into account Fig. 12, and a small number of SF and AGN sources in the most central part of cluster, our results are in line with previous findings which suggest that the number of SF galaxies (e.g. Gómez et al. 2003; Christlein & Zabludoff 2005; Hansen et al. 2009; von der Linden et al. 2010) and AGN (e.g. Gavazzi, Savorgnan & Fumagalli 2011; Davies et al. 2017; Marshall et al. 2018; Koulouridis & Bartalucci 2019; Li et al. 2019) decreases towards the cluster centre. The majority of SF galaxies and AGN found in this work are distributed at cluster-centric distances $>$ 1.3 Mpc. Moreover, the results obtained by Deshev et al. (2017) while analysing the evolution of galaxies in merging clusters with special focus on A520 at $z = 0.2$, indicate that the core of such

Downloaded from https://academic.oup.com/mnras/article/501/2/2430/6031334 by guest on 12 February 2026

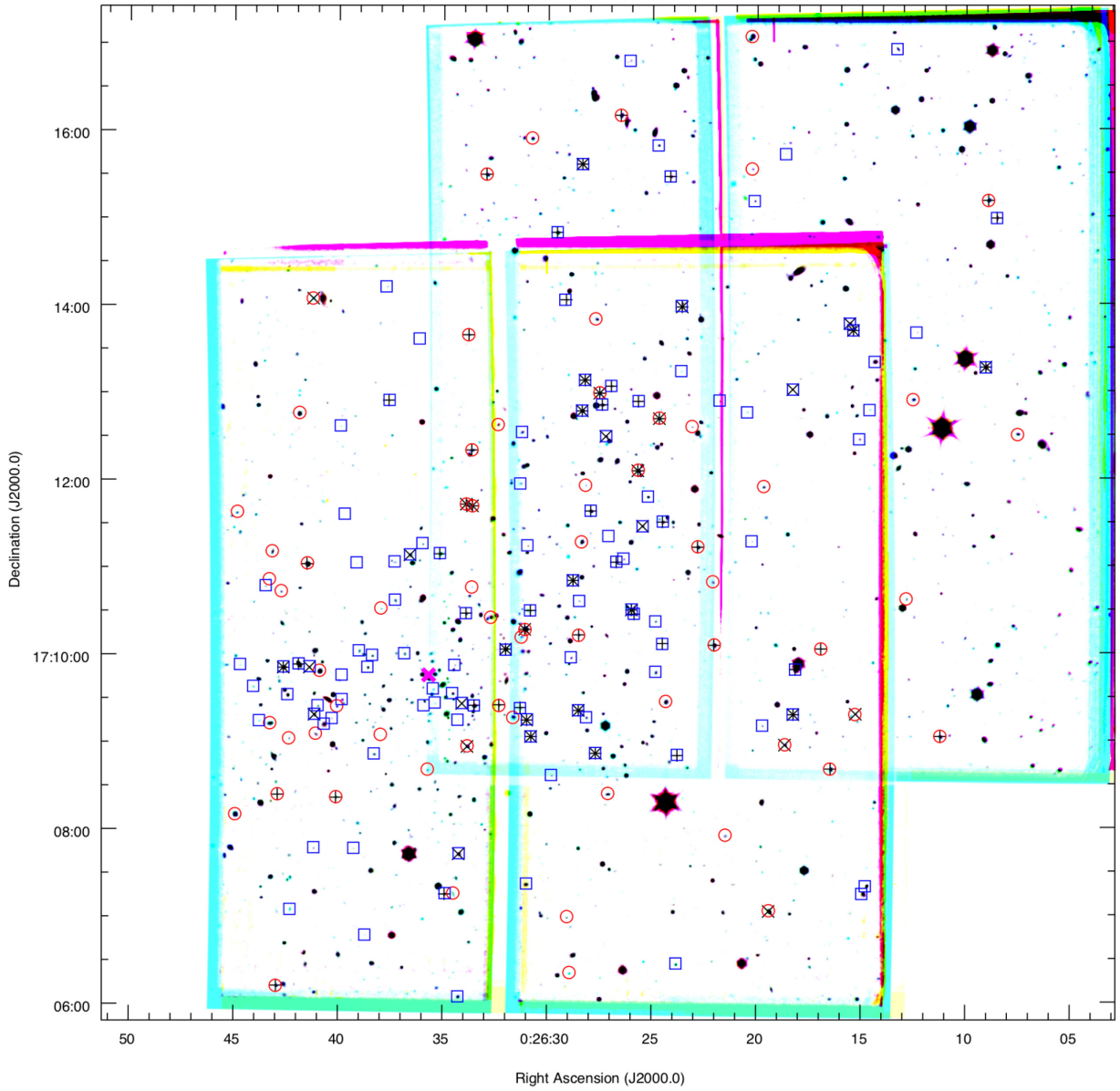


Figure 8. RGB mosaic (H α, [O III], and H β, respectively) of the OSIRIS/GTC deep images of ZwCl0024+1652. The blue squares correspond to SF galaxies and red circles represent AGN hosts, as provided by Sánchez-Portal et al. (2015). The 'X' symbols denote [O III] emitters while '+' signs represent H β ELGs from our work. The magenta cross ($\times$) denotes the centre of the cluster (galaxies/BCG).

clusters up to a cluster-centric distance of 1.5 Mpc is almost devoid of SF galaxies. Since it is well known that ZwCl0024+1652 cluster is a merging cluster (Czoske et al. 2002; Jee et al. 2007), our findings confirm the existing results.

6.2 Colour and stellar masses

In this section, we discuss some of the galaxy parameters such as colours and stellar masses, in relation to the SF and AGN properties. To begin with, we plotted a colour–magnitude diagram (CMD) for the cluster emitters detected in both [O III] and H β, with public photometric data gathered from Treu et al. (2003) and Moran et al. (2005). We applied the *k*-correction (Blanton & Roweis 2007) to the observed magnitudes to get the rest frame $B - R$ colour and the absolute magnitude in B. Fig. 13 shows the relation between these variables for all [O III] and H β emitters. To separate a blue cloud (BC) and red sequence (RS) we introduced a horizontal line at $B - R = 1.39$ as given by Sánchez-Portal et al. (2015). We determined that only 6 sources (9 per cent) would belong to the RS while majority (64) of the sources (91 per cent) remain in the BC region, as expected. The plot includes distributions of both analysed parameters. We do not find any significant difference in the distribution of [O III] and H β lines, and most of the sources in both cases (85 per cent for [O III] and 97 per cent for H β) are in the BC, as expected. For the galaxies identified on the CMD, 27 and 13 H β emitters are LT and ET, respectively. In the case of [O III] emitters 14 and 8 sources have LT and ET morphologies, respectively. A total of 69 galaxies have spectroscopic classification available, where 42 (60 per cent) and 27 (40 per cent) galaxies are SF and AGN, respectively.

Stellar mass is another parameter that plays an important role in determining different galaxy parameters such as SFR and sSFR. Previous studies at different redshifts (from the local Universe to

Downloaded from https://academic.oup.com/mnras/article/501/2/2430/6031334 by guest on 12 February 2026

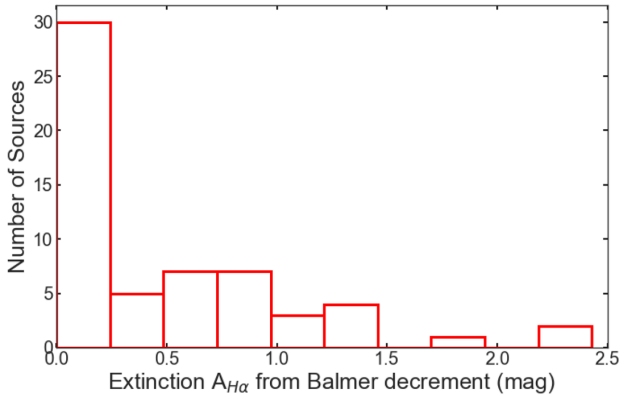


Figure 9. Distribution of extinctions derived from the Balmer decrement, assuming a galactic extinction law of Seaton (1979).

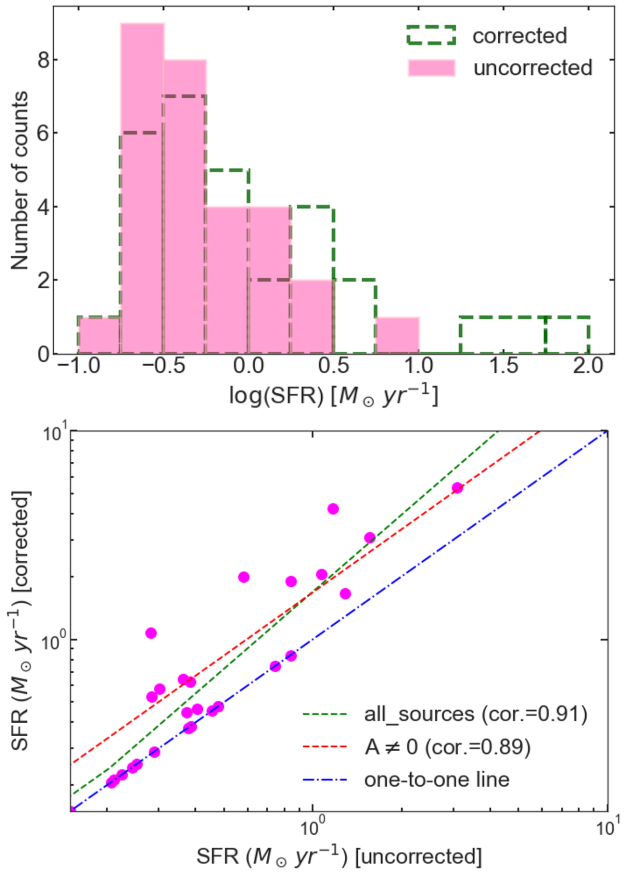


Figure 10. Top plot: Distribution of corrected and uncorrected SFR. Bottom plot: Relation between extinction corrected and uncorrected SFR for ZwCl0024+1652, according to the details given in Section 5.4. The blue dash-dotted and green dashed lines show one-to-one correlation and linear fit for all sources, respectively. While the red dashed line represents the linear fit for those galaxies with zero extinction.

$z \sim 2$) confirm that stellar mass plays a leading role in determining SFR (e.g. Koyama et al. 2013; Darvish et al. 2016; Laganá & Ulmer 2018; Pintos-Castro et al. 2019). Using a sample of SDSS galaxies in groups, Li et al. (2019) reported higher SF fractions at all cluster-centric distances for lower stellar masses, and higher stellar masses of AGN host galaxies. Moreover, at higher redshifts ($z \sim$ 1–2) lower

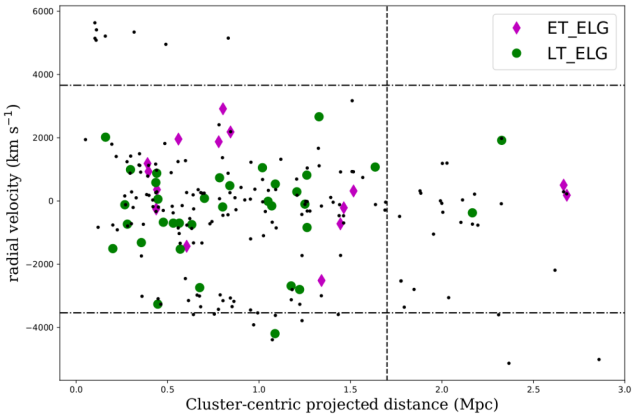


Figure 11. Radial velocity versus cluster-centric distance for H β and [O III] ELGs with morphological classifications. The magenta diamonds represent ETs while green dots correspond to LT galaxies. The virial radius (r_{vir} = 1.7 Mpc) (Treu et al. 2003) is represented by dotted vertical line. The dashed-dotted horizontal lines stand for the radial velocity limits fully covered within the field of view of the two OSIRIS TF pointings. The small black points correspond to ELGs with H α emission from Sánchez-Portal et al. (2015).

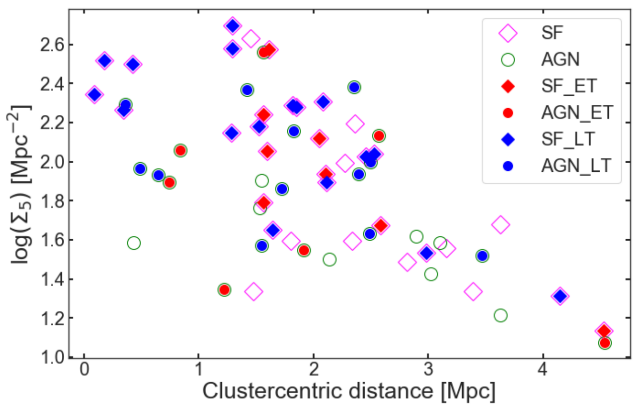


Figure 12. Dependence of the local density on the cluster-centric distance of all SF galaxies (magenta open diamonds) and AGN (green open circles) that belong to the main cluster structure. The blue and red symbols stand for LT and ET galaxies, respectively.

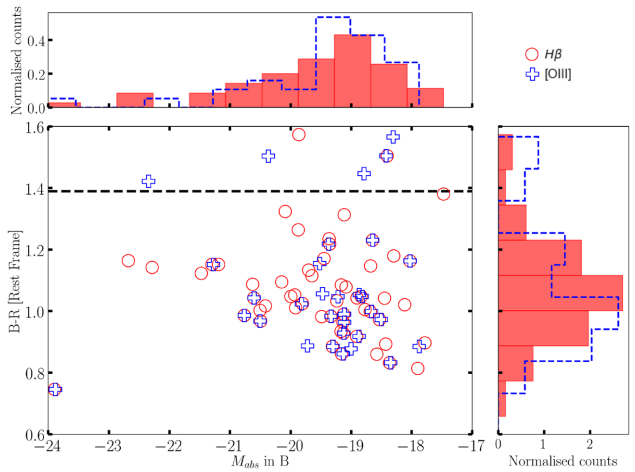


Figure 13. B – R rest-frame colour versus absolute magnitude M_B, for the case of ZwCl0024+1652. The blue crosses represent [O III] emitters while red circles stand for H β emitters.

Downloaded from https://academic.oup.com/mnras/article/501/2/2430/6031334 by guest on 12 February 2026

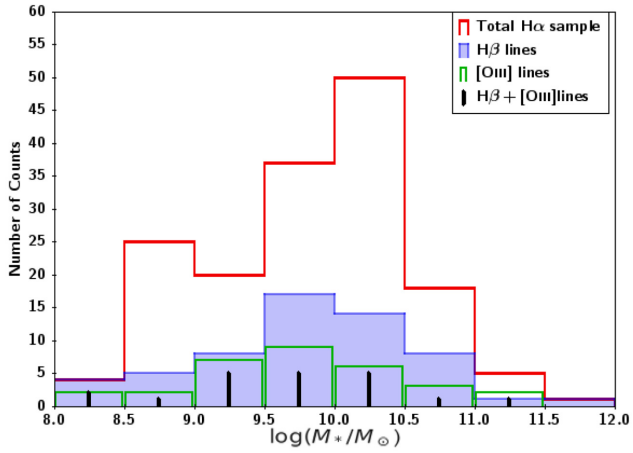


Figure 14. Distribution of the stellar masses. The base sample (H α emitters) is represented with red lines, H β lines with blue shaded bars, [O III] emitters with green lines and the black lines represent galaxies with both H β and [O III] emission.

Table 8. Statistical description of stellar masses ($\log(M_*/\mathrm{M}_\odot)$) of our base H α sample (Sánchez-Portal et al. 2015) with consecutive identification of H β and [O III] emissions.

$\log(M_*/\mathrm{M}_\odot)$ of	Q_1	Median	Q_3
H α base sample	9.16	9.97	10.39
H β line emitters	9.22	9.82	10.39
[OIII] line emitters	9.22	9.82	10.39
Both H β+[O III] line emitters	9.16	9.82	10.39

masses of galaxies in clusters are accompanied by enhanced star formation (e.g. Brodwin et al. 2013; Alberts et al. 2016) with a peak value at $M_* \simeq 10^{9.8}\,\mathrm{M}_\odot$ (Patel et al. 2011). In our case, the stellar mass was computed for each cluster galaxy with `LePhare` code using BC03 templates, as mentioned in Section 4.3. The mass distribution of our base sample (H α sample) and consecutive subsamples (H β and [O III] emitters) is presented in Fig. 14 and statistically described in Table 8. From Table 8 we can see that the mass distributions for the base sample and consecutive ELG samples are similar, with 50 per cent of the sample having masses in the range about 9.20 – 10.39 in all cases, with median of $\sim$ 9.9. From the histogram (Fig. 14) and the statistics we can see that our consecutive samples cover a complete range of masses from the base H α sample. In the following paragraphs, we discuss different galaxy properties in relation to the effects of stellar mass.

In the first place, we have investigated the behaviour of the SFR and sSFR with stellar mass, as depicted in Fig. 15. Following Laganá & Ulmer (2018), we further discern between active star-forming galaxies and those in quenching phase, both in field and cluster environments. For this purpose, we used the redshift-dependent sSFR cut, such that $\mathrm{sSFR}(z) = 10^{-10} \times (1+z)^3$, given by Koyama et al. (2013) and the result for cluster galaxies is summarized in Table 9. In Fig. 15, representative average error bars are shown in the plots with average values being 9.37, 0.587, and −10.09, for $\log(M_*/\mathrm{M}_\odot)$, log (SFR) and log (sSFR), respectively. The upper and the lower error limits are determined for each of these parameters. We have observed a rather different behaviour in active SF and quenched galaxies; on the one hand, the distribution of quenched galaxies extends to higher masses than that of active SF ones, in good agreement with previous results; on the other, we observed that the $\log(M_*/\mathrm{M}_\odot)$–log(SFR) relation of active SF galaxies can be well fitted by a straight line roughly parallel to the main sequence of SDSS SF galaxies (and to that of field galaxies at similar redshift; see Section 6.4); however, for quenched galaxies there is a much larger dispersion of values so a linear fit is not appropriate; the behaviour of the sSFR is again remarkable: the sSFR declines mildly with stellar mass for active SF galaxies, but for quenched galaxies this trend is really outstanding, indicating a strong reduction of the SF efficiency with stellar mass. The SFR–M_* correlation in our results, and the anticorrelation of sSFR with M_* conforms with existing results (e.g. Vulcani et al. 2010; Speagle et al. 2014; Vulcani et al. 2015; Guglielmo et al. 2019, and references therein). Concerning the morphologies of SF galaxies, the number of classified galaxies is very low, especially when dealing with ETs. In general, most of LT galaxies are observed to be located slightly below the SDSS main sequence of SF, while the existing small number of ETs has been found above the line.

Secondly, we have studied the dependence of the SF and AGN fractions on the stellar mass. The distributions of stellar masses of our sample of ELGs and that of the ancillary H α cluster catalogue follow a similar, bimodal profile with two local maxima at the low- and high-mass ends. The low-mass maximum is placed around $\log(M_*/\mathrm{M}_\odot) = 9$ for both distributions. The high-mass local is placed at $\log(M_*/\mathrm{M}_\odot) \simeq 9.8$ and $\simeq 10.5$ for our ELGs and the overall population, respectively. The mass distributions of the overall H α emitting cluster sample and our ELGs are presented in Fig. 16.

We finally discuss the effect of stellar masses to the SF and AGN fractions. Within the footprint of the GLACE observations, we have 359 galaxies in the ancillary catalogue of cluster members with derived stellar masses; we have divided the sample into three bins, namely low- ($\log(M_*/\mathrm{M}_\odot)) < 9.5$), medium- ($9.5 \leq \log(M_*/\mathrm{M}_\odot)) < 10.5$), and high-mass ($\log(M_*/\mathrm{M}_\odot)) \geq 10.5$) with 109, 135, and 115 galaxies, respectively. The fraction of SF galaxies as a function of the stellar mass and local density is described in the coming section. There is a strong decline in the fraction of SF galaxies in the high-mass bin, confirming that SF is highly suppressed in cluster high-mass galaxies. This agrees with results of Stasińska et al. (2015) whose study implemented the BPT and WHAN diagrams (Cid Fernandes et al. 2011). For high mass bin, the small fraction of SF galaxies in our cluster could be because the galaxies in this bin could have formed almost all the stars at redshifts higher than $z \sim 0.4$. Finally, the fraction of AGN galaxies as a function of the stellar mass and local density is presented in the following section. There is a slight decline of the fraction of AGNs both at the low- and high-mass bins, although not very significant.

6.3 The phase–space relation and the local density effects

We adopted the centre coordinates of the cluster as $\mathrm{RA_c} = 0^{\mathrm{h}}26^{\mathrm{m}}45.9^{\mathrm{s}}$ and $\mathrm{DEC}_c = 17^{\mathrm{d}}\,9^{\mathrm{m}}41.1^{\mathrm{s}}$, based on the work of Diaferio, Geller & Rines (2005). Taking into account the distance of the cluster of 1500 Mpc and following the procedure outlined in Beyoro-Amado et al. (2019), we computed the cluster-centric distance of each identified ELG. The radial velocity was also computed and the phase–space diagram was plotted to identify the distribution of the sources (both [O III] and H β emitters) as shown in Fig. 5. We limited the sample to the main structure of the cluster ($0.385 < z < 0.41$) and excluded the BLAGN galaxies as described in Section 5.3. The resulting distributions of H β and [O III] line emitters in cluster-centric distance are given in Fig. 17. Moreover, the phase–space diagram with two plots (for H β and [O III]) showing the line of site velocity versus the projected cluster-centric distance is introduced in Section 5, Fig. 5. Combining the relationships observed

Downloaded from https://academic.oup.com/mnras/article/501/2/2430/6031334 by guest on 12 February 2026

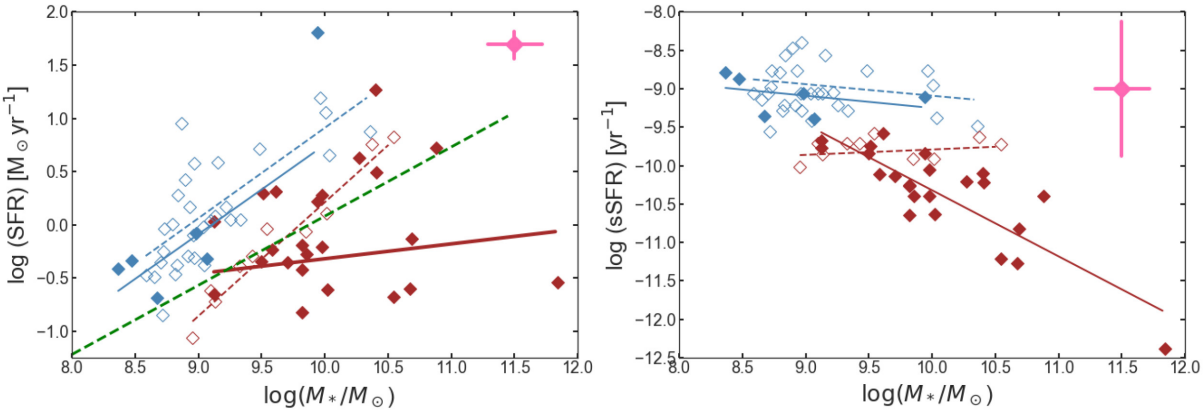


Figure 15. Dependence of the SFR (left-hand panel) and sSFR (right-hand panel) on the stellar mass (log (M_*/M$_\odot$)) for cluster galaxies (filled diamonds with solid linear fittings) and for field galaxies (open diamonds with dashed linear fittings) at $z \sim 0.4$. Active SF and quenching-phase SF galaxies are discriminated with blue and brown colours, respectively. A representative average error bar for cluster SF galaxies is indicated in each plot with pink colour. The dashed green line (left-hand panel) shows the SF main sequence of SDSS galaxies.

Table 9. Summary of the placement of our sample SF galaxies into active or quenching phase.

Class	Cluster	Field
Active SF	6 (21 per cent)	30 (75 per cent)
Quenching SF	23 (79 per cent)	10 (25 per cent)
Total SF	29 (100 per cent)	40 (100 per cent)

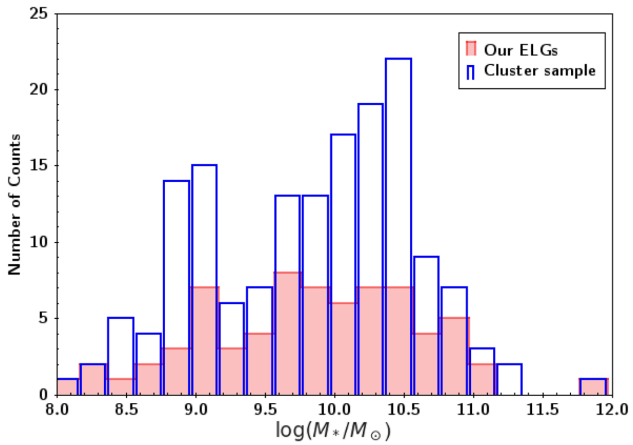


Figure 16. Distribution of our H β and/or [O III] ELGs (red filled histograms) and H α cluster sample (blue open histograms).

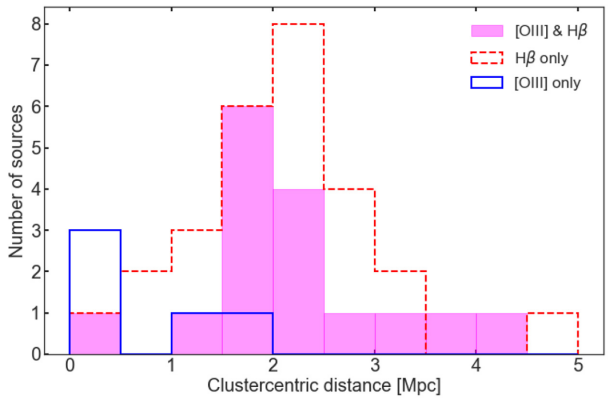


Figure 17. Distribution of [O III] and H β emission lines in ZwCl0024+1652 cluster with cluster-centric distance, for members of the main cluster structure.

from both informations (cluster-centric distance distribution and phase–space diagrams) one can comment on the location of member galaxies inside the cluster (e.g. Jaffé et al. 2015). From the plots in Figs 5 and 17 it can be seen that [O III] emitters are relatively closer to the cluster centre than H β line emitters despite all our emitters are with in r_{vir} of our cluster. One of these sources has one of the highest dust extinctions ($A_{H\alpha} = 2.43$ mag). For the remaining three [O III]-only SF galaxies we estimated extinctions using the H β limiting flux given in Table 5, obtaining $A_{H\alpha}$ values between 1 and 2 mag. This fact could explain the lack of H β detection for those objects. On the other hand, we verify that about half of [O III]- and H β-only emitters are located in intermediate cluster-centric distances. The lack of [O III]-only emitters at large cluster-centric distances is intriguing, however we would need larger samples to confirm this and to understand the possible cause.

For discussion related to environment concentrating in the main cluster structure, we found 35 SF galaxies and only 13 AGNs within the cluster-centric distance range of 0–5 Mpc. Despite the small number statistics, we found that the AGN hosts belonging to the main structure of the cluster are concentrated inside $\sim$1.5 virial radii ($\sim$3 Mpc). This contrasts to the results given by Sobral et al. (2016), who did not find any strong dependence of AGN fraction on environment for the case of Cl 0939+4713 at $z \sim 0.4$. To support our results, we presented a phase–space relation in Fig. 5 clearly representing the distribution of SF and AGN galaxies with [O III] and H β emission lines. Our findings are in line with previous results at intermediate redshifts reporting that the fraction of AGN increases with cluster-centric distance, confirming the environment dependence on AGN activity (e.g. Hora & Xinyu 2009; Argudo-Fernández et al. 2018; Koulouridis & Bartalucci 2019). On the other hand, SF galaxies are distributed across all measured cluster-centric distances, but they are preferentially located between 0.5 and 1.5 virial radii, with the bulk of SF galaxies exhibiting the lowest extinction values.

We computed a valid local density estimation for 72 from 73 sources of the main cluster sample using the algorithm from Dressler et al. (1985). We also computed the local surface density with

Downloaded from https://academic.oup.com/mnras/article/501/2/2430/6031334 by guest on 12 February 2026

the same approach for VVDS-Deep field SF galaxies selected as described in Section 2.3. Fig. 18 describes the relationship of SFR and sSFR to local density where it is shown separately for active as well as quenching phase SF galaxies. Previous studies suggested that, both in the local Universe and at higher redshift, regions with higher projected local density are generally characterized by smaller fractions of galaxies with ongoing star formation (e.g. Pimbblet et al. 2002; Gómez et al. 2003; Kauffmann et al. 2004). On the other hand, different works have shown that SF could be triggered and/or quenched by the nature of environment in which the galaxy is located, as can be described through relations between different parameters (such as colour, morphology, stellar mass, and SFR) and environment (e.g. Peng et al. 2010, 2012; Tomczak et al. 2019, and references therein). Poggianti et al. (2008) used the [O II] emission line as a proxy of the SFR of galaxies in clusters in the range $0.4 < z < 0.8$, showing that the SFR is lower in denser environments (see also Rudnick et al. 2017). Recently, Laganá & Ulmer (2018) derived the SFR of cluster galaxies at $0.4 < z < 0.9$ from broad-band SED fitting, and found no clear dependence between either SFR or sSFR and local environment. Pintos-Castro et al. (2013) also studied the dependence of the SF activity derived from IR luminosity with local environment in a young galaxy cluster at $z \sim 0.87$, finding that the average SFR and sSFR are roughly independent of the local environment. However, the fraction of SF galaxies varies with the local density, being enhanced in the intermediate density regions and dropping in the highest local density ones. The same behaviour is observed in both high- and low-mass galaxies. From the projected phase space diagrams in Figs 5 and 11 we have determined that the most central region of the cluster ($r \lesssim 0.3$ Mpc) is almost devoid of ELGs, leading to a conclusion that the star formation and the AGN activity could be completely quenched. We can also deduce that almost all ELGs are located in the main cluster structure (structure 'A'). In a recent work, Pintos-Castro et al. (2019) further studied the population of SF galaxies within a sample of IR-selected galaxy clusters in the range $0.3 \leq z \leq 1.1$ by means of broad-band SED fitting, finding a decrease of the fraction of SF galaxies from field towards cluster cores, strongly dependent on stellar mass and redshift.

The relations among SFR and galaxy environment have been studied by many authors in our redshift range (e.g. Vulcani et al. 2010; Stroe et al. 2015). In this work, we have explored the SF activity (as given by the SFR and sSFR) for the purely SF galaxies (after removing AGN sources) as a function of the environment, as depicted in Fig. 18. No clear correlation between the SFR and local density is observed for either active SF or quenched cluster galaxies, in line with previous results. However, for the sSFR we found a remarkable behaviour: the sSFR seems to be correlated with local density for active SF galaxies, and anticorrelated for quenched ones. While the former relation is mild and could be impacted by the small size of the subsample (five galaxies), the latter seems to be stronger and supported by the larger size of the set of quenched galaxies. Even though there is a mild, highly dispersed correlation between stellar mass and local density that can somehow contaminate the result, this finding suggests that star formation efficiency declines with the increase of the local density of the environment. Moreover, this trend, but with a slope about 1.4 times shallower, has been also reported by Chung et al. (2011) in a comprehensive study of a sample of 69 clusters at $z < 0.1$. Hence, this suggest a possible evolution of the quenching strength of SF galaxies, which evidently requires further studies. Moreover, morphologies of the SF galaxies have been observed against active and quenching SF phases. In active SF phase, 33 per cent of galaxies with known morphologies are ET while 67 per cent are LT. Similar has been found for quenching SF phase, where 37 per cent and 63 per cent of sources are ET and LT, respectively. Our results show that getting into quenching phase from active SF phase, the ET and LT proportions look nearly the same (with slight increase of ET fraction with a slight decrease in LT proportion); not exactly conforming with previous results (e.g. Kelkar et al. 2019) showing relatively suppressed star formation in older stellar populations. That could be because of small statistics in this work.

Finally, in order to investigate the dependence of the fraction of SF galaxies on stellar mass and the environment, we have described the SF fractions as a function of stellar mass (right-hand panel) and with local density Σ_5 (left-hand panel) of Fig. 19. As in Pintos-Castro et al. (2013), we have followed the prescription of Koyama et al. (2008), who defined the intermediate density environment as a relative narrow range of local density where the optical colour distribution starts to change dramatically. According to their definition, the low-density environment corresponds to $\log \Sigma_5 < 1.65$, the medium-density range to $1.65 \leq \log \Sigma_5 < 2.15$ and finally the high-density range to $\log \Sigma_5 \geq 2.15$. Pintos-Castro et al. (2013) demonstrated that the derived parameters are robust against small random variations of the boundaries, and therefore the selection does not condition the results of the environmental analysis. The total number of objects from the ancillary cluster catalogue within the sky area of our survey and with $R_{\rm AB} < 23$ are 86, 139, and 222 in the low-, medium-, and high-density bins, respectively. The fractions were computed as the ratio of the number of SF galaxies in each bin to the total number of member galaxies in the same bin. The uncertainty in each fraction was computed as the ratio of the fraction in the bin to the square root of the total number of galaxies in that bin. It can be observed that the fraction of SF galaxies smoothly declines across the low- and medium-density bins, dropping towards the high-density region. Hence, we cannot support the claim of Pintos-Castro et al. (2013) that the intermediate density environment favours the enhancement of the SF activity, although it does not inhibit it (or quenching and triggering effects compensate). Authors of Pintos-Castro et al. (2013) gave results based on low $\log(M_*/{\rm M}_\odot) < 10.5$ and high ($\log(M_*/{\rm M}_\odot) \geq 10.5$) mass bins, concluding that high density regions have scarcity of low mass SF galaxies. Moreover, they reported that high sSFR values are observed in low density regions, where high mass systems characterized by low sSFR dominate the high density environment. While examining our results in high and low mass bins as in Pintos-Castro et al. (2013) we observed significant number of low mass SF galaxies. In addition to this, we found that low mass SF galaxies posses high sSFR independent of environment while high mass SF galaxies in high density region have low sSFR values. Using the same bins and a similar procedure, we computed the AGN fraction, as shown in Fig. 20 right-hand panel for its dependence on stellar mass while left-hand panel describing the variation with local density, finding a similar trend as for SF galaxies, i.e. declining throughout the low- and medium-density environments and dropping sharply at higher densities. This is in line with previous results (e.g. Li et al. 2019). The mean local densities of SF galaxies and AGN are $\log(\Sigma_5)\ [{\rm Mpc}^{-2}] = 2.00 \pm 0.39$ and 1.82 ± 0.34, respectively.

6.4 Cluster-field comparison at $z \sim 0.4$

Both the field and cluster galaxies are consistently selected in a similar approach. Fig. 18 shows that both are quite smoothly distributed in a local density range covering ~ 5 decades. We are confident that GLACE data also reasonably samples the lower density outskirts of this cluster out to $\sim 2r_{vir} \approx 4$ Mpc (with OSIRIS TF

Downloaded from https://academic.oup.com/mnras/article/501/2/2430/6031334 by guest on 12 February 2026

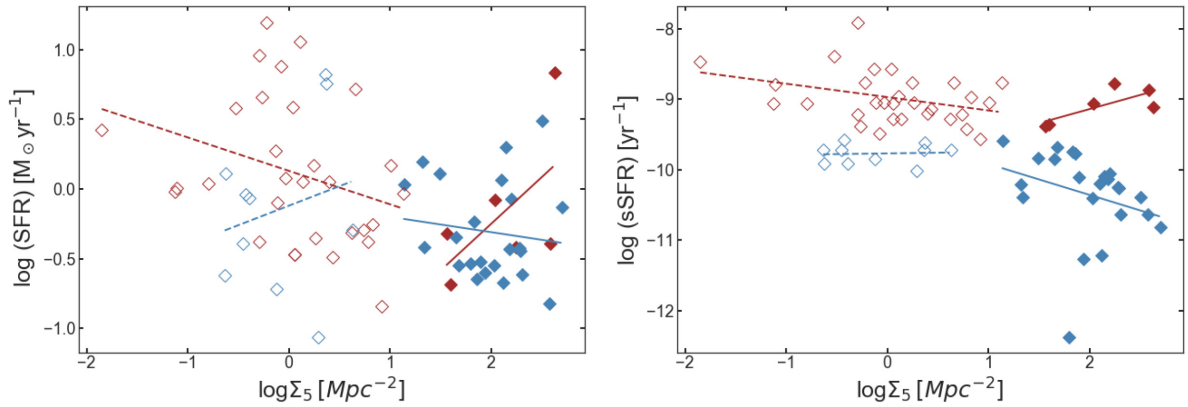


Figure 18. Dependence of the SFR (left-hand panel) and sSFR (right-hand panel) on the local density (Σ_5) for cluster galaxies (filled diamonds with solid linear fittings) and for field galaxies (open diamonds with dashed linear fittings) at $z \sim 0.4$. Active SF and quenching-phase SF galaxies, separated as described in Section 6.2, are discriminated with brown and blue colours, respectively.

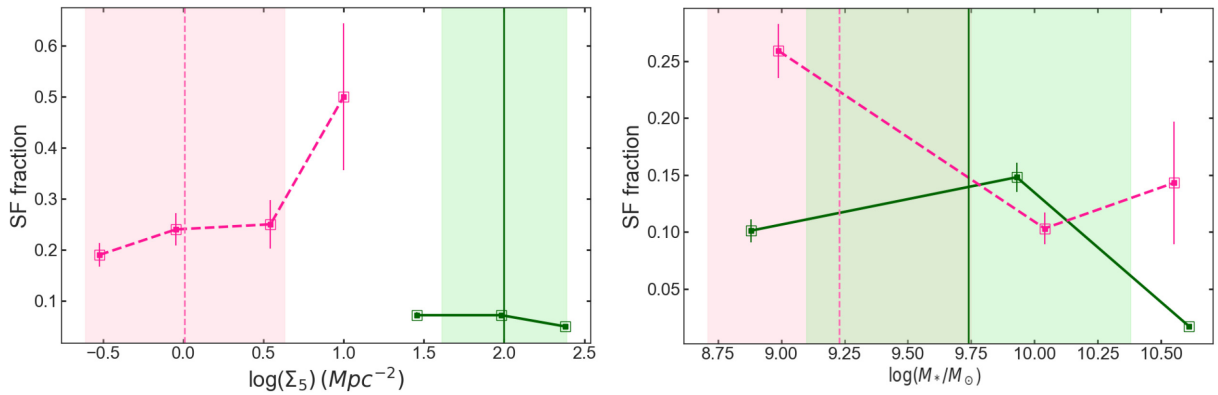


Figure 19. Variation of the fraction of SF galaxies versus local density (left-hand panel) and stellar mass (right-hand panel). The solid green lines show cluster galaxies and the pink dashed lines show field galaxies at $z \sim 0.4$. In the right-hand panel, the sample is divided into three mass bins with low: $\log(M_*/\mathrm{M}_\odot) < 9.5$, medium: $9.5 \log(M_*/\mathrm{M}_\odot) < 10.5$ and high: $\log(M_*/\mathrm{M}_\odot) > 10.5$. Error bars correspond to Poissonian statistics (see the text). Vertical lines represent the corresponding mean values with a light shaded standard deviation.

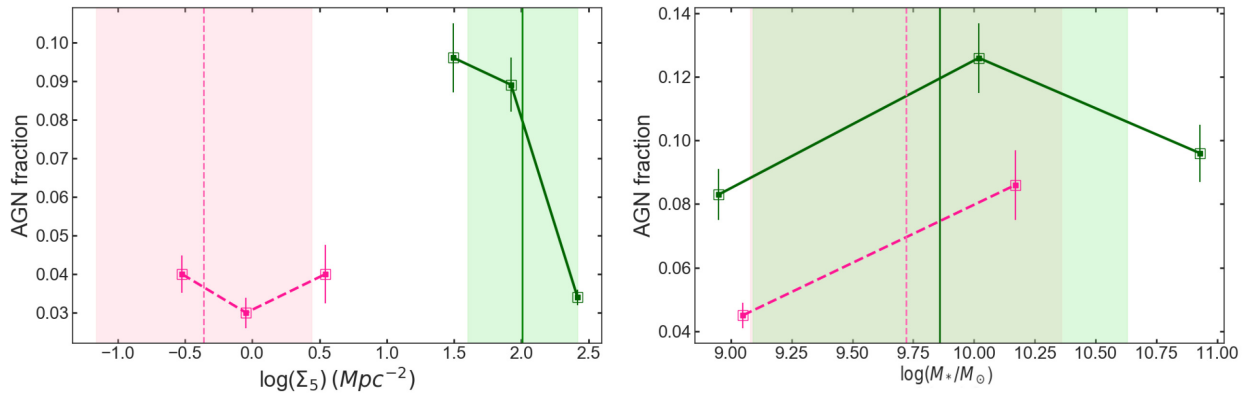


Figure 20. Variation of the fraction of AGN galaxies versus local density (left-hand panel) and stellar mass (right-hand panel). The solid green lines show cluster galaxies and the pink dashed lines show field galaxies at $z \sim 0.4$. In the right-hand panel, the sample is divided into three mass bins with low: $\log(M_*/\mathrm{M}_\odot) < 9.5$, medium: $9.5 \leq \log(M_*/\mathrm{M}_\odot) < 10.5$ and high: $\log(M_*/\mathrm{M}_\odot) > 10.5$. Error bars correspond to Poissonian statistics (see the text). The vertical lines represent the corresponding mean values with a light shaded standard deviation.

giving a circular FOV of 4 arcmin radius), despite the angular coverage of our observations is not exhaustive. We assume that VVDS data are fairly representative of field galaxies at the cosmic epoch studied here.

Evidence from large-area surveys (e.g. Gómez et al. 2003; Bongiovanni et al. 2005) shows that the volume-averaged SFR monotonically decreases with higher environmental densities. In particular, higher average SFRs are found in the field at different

Downloaded from https://academic.oup.com/mnras/article/501/2/2430/6031334 by guest on 12 February 2026

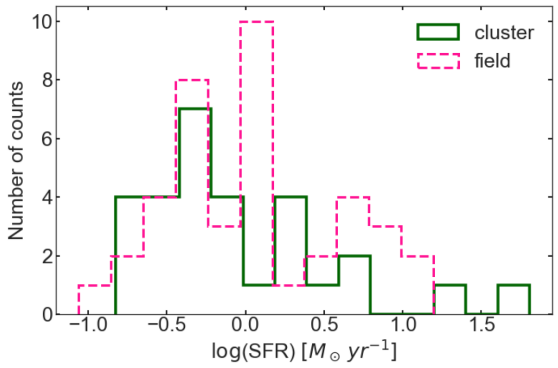


Figure 21. Histogram representing the distribution of SFR for SF galaxies in ZwCl0024+1652 (green solid) and field (dashed pink) lines. The mean value of log(SFR) [$M_\odot\ yr^{-1}$] = −0.06 ± 0.60 for cluster members while the mean log(SFR) [$M_\odot\ yr^{-1}$] = 0.05 ± 0.054.

redshifts from $z\sim1$ when compared to galaxy cluster environments (e.g. von der Linden et al. 2010; Muzzin et al. 2012; Paulino-Afonso et al. 2018; Hwang, Shin & Song 2019). At higher redshifts, SFRs of cluster galaxies showed to be greater than in the case of field galaxies (e.g. Tran et al. 2010; Alberts et al. 2014). In Fig. 21 we show a comparison of SFRs of the ZwCl0024+1652 cluster and field galaxies from VVDS at the same cosmic epoch. A global difference of ∼0.1 dex between both sets, with higher SFRs obtained for field galaxies than cluster members, according to the results referred above.

Regarding the relation between the SFR and the local density (Σ_5), it is not clear whether there exists a significant change of the SFR with this parameter for both, cluster and field environments, independently from their evolutionary phase, as shown in the left-hand panel of Fig. 18. In contrast, the environmental dependences of the sSFR are clearer, as shown in the right-hand panel of Fig. 18. In fact, the ratio of field active SFGs to quenching (or transient) phase ones in the sSFR−Σ_5 relation is turned upside down with respect to that of the cluster. At redshift $z\ \sim\ 0.4$, we found ∼ 21 per cent (∼ 79 per cent) and ∼ 75 per cent (∼ 25 per cent) of active SFGs (quenching phase) cluster and field galaxies, respectively. Hence, while in low density environments there is a relatively low fraction of transient SF galaxies without a measurable dependence on the local density, in the case of this cluster we found a remarkable environment-depending SF quenching, as already mentioned in Section 6.3. This finding agrees with previous studies carried out at different redshifts (e.g.) Cucciati et al. (2017), who used VIMOS Public Extragalactic Redshift Survey (VIPERS) to analyse environmental effect on the evolution of galaxies at $0.5 \leq z \leq 0.9$, Baldry et al. (2006) for environment studies carried out in the local Universe, and Cucciati et al. (2010) for intermediate redshift studies, but in galaxy groups. All of these studies have found in common that the ratio of active to quenching SF galaxies is smaller in higher density environments. The mean fraction of the field SFGs is comparable with that of cluster in the low-density regime, as illustrated in Fig. 19.

About the relationships with stellar mass, there is a well-established relation between this parameter and SF phenomena, both in field and cluster (e.g. Noeske et al. 2007; Lara-López et al. 2010; Peng et al. 2010; Speagle et al. 2014). In general, the SFR–M_* relation has a bivariate behaviour depending on the SF activity. The active SF galaxies populate the main sequence, whereas the quenched (e.g. post-starbursts) ones tend to be grouped horizontally in this diagram.

In Fig. 15 (left-hand panel) we show the dependence of SFR on stellar mass both for field and cluster SFGs. Accordingly, log (SFR) and log ($M_*/M_\odot$) are positively correlated with slopes 0.12 / 0.64, respectively for cluster/field SF galaxies. As a reference, we have represented the main sequence (MS) traced by low-redshift SFGs from SDSS (Brinchmann et al. 2004). The active SF galaxies of the cluster tends to populate a region that roughly corresponds to the MS, especially for large masses, while active SF and a few galaxies in quenching phase of the field reside above it.

From the definition given above, the sSFR traces the contribution of the star-formation processes to the mass growth of the galaxies. In general, low-mass galaxies tend to have higher sSFR than their high-mass counterparts (see Vulcani et al. 2010, and references therein). This is just one of consequences of the 'downsizing' scenario, which favours the formation of massive galaxies in earlier epochs and shorter time-scales and the opposite situation for low-mass galaxies. From Fig. 15 (right-hand panel) it can be seen that a general inverse relation is observed between the log (sSFR) and log ($M_*/M_\odot$), both field and cluster, in agreement with this scenario but at different mass scales and the same cosmic epoch. This fact suggest that the cluster environments favours a rapid transition from active SF to quenched phase compared with the field. In other words, the high-density environments at intermediate redshifts are real laboratories for testing the properties of low-redshift galaxies of high mass.

Finally, despite the relatively small statistics in the field sample, we can clearly see that irrespective of the local density values the SF fraction in the core of the cluster is around a half of that in the field environment. On the other hand, the trend of the SF fractions of field galaxies as a function of stellar mass is opposite to that of cluster galaxies. This suggests an accelerated evolution of cluster galaxies with respect to field ones. In contrast, the AGN fractions as a function of M_* have the same trend.

7 CONCLUSIONS

In this work we are demonstrating the capabilities of tunable filters (TF) to study ELG populations in galaxy clusters. We focused our study on ZwCl0024+1652 cluster at an intermediate redshift of $z\ \sim$ 0.4, observed using the GTC/OSIRIS instrument under the GLACE survey. This paper describes TF observations, data reduction, sample selection, and analysis of [O III] and H β emission lines. We compared the obtained fluxes and luminosities of [O III] and H β lines with H α and [N II] lines measured in Sánchez-Portal et al. (2015). We studied different properties of [O III] and H β emitters in terms of their cluster-centric distance, morphology, star formation, AGN activity, local density, and stellar mass. Finally, we compared the properties of our cluster galaxies with the field galaxies at the same redshift using data from the VVDS-Deep survey. Our main findings are:

(i) Out of 174 previously confirmed H α emitters (Sánchez-Portal et al. 2015), 35 (∼ 20 per cent) and 59 (∼ 34 per cent) galaxies show [O III] and H β emission lines, respectively, out to the H α flux of 2.43×10^{-15} erg s^{-1} cm^{-2}. Our TF redshifts computed from the position of H β and [O III] lines using the pseudo-spectra have been compared with previous results of Sánchez-Portal et al. (2015), finding a good correlation between all measurements.

(ii) For 20 galaxies we were able to reproduce the BPT-NII diagram finding 8 (40 per cent) SF galaxies, 11 (55 per cent) composites, and 1 (5 per cent) LINER. In terms of morphology, we found higher fraction of LT (∼ 67 per cent) sources in comparison to

Downloaded from https://academic.oup.com/mnras/article/501/2/2430/6031334 by guest on 12 February 2026

ETs (∼ 33 per cent), showing that ELG are predominantly late-types with SF and/or AGN activity going on.

(iii) From the projected phase–space and the cluster-centric distance analysis, we determined that core of this cluster is relatively free of ET galaxies with emission lines up to the cluster-centric distance of ∼ 500 kpc.

(iv) We found that both SF galaxies and AGN follow the local density-cluster-centric distance anticorrelation, and we confirmed using TF observations that cores of regular galaxy clusters are poor with SF galaxies and AGN up to the cluster-centric distance of ∼ 1.3 Mpc. This is in line with most of previous studies where SF and AGN activity has been detected using other than TF data.

(v) The sSFR seems to be anticorrelated with local density for quenched galaxies, suggesting that the star formation efficiency declines with the increase of local density of the environment.

(vi) The fraction of SF galaxies and AGNs remain roughly constant across the low- and medium-density environments, dropping sharply towards high-density environments.

(vii) The distribution of quenched galaxies extends to higher masses than that of active SF ones. The $\log(M_*/M_\odot)$–log(SFR) relation of active SF galaxies can be well fitted by a straight line roughly parallel to the main sequence of SF galaxies.

(viii) The sSFR declines mildly with stellar mass for active SF galaxies, but for quenched galaxies this trend is really outstanding, indicating a strong reduction of the SF efficiency with stellar mass.

(ix) There is a strong decline in the fraction of SF galaxies in the high stellar mass range, confirming that SF is highly suppressed in cluster high-mass galaxies. However, no remarkable trend with respect to stellar mass is observed for AGNs.

(x) Cluster-field comparison in terms of star formation processes suggest an accelerated evolution of galaxies in cluster with respect to field.

This work provides an important contribution to previous studies regarding the properties of emission line galaxies in clusters, and shows the importance and strength of TF data to study galaxy clusters even at higher redshifts. An example of catalogue with properties of detected emission line galaxies is given in Appendix of this paper, while the full catalogue will be available in the electronic version.

ACKNOWLEDGEMENTS

We acknowledge the anonymous referee for helpful comments and valuable suggestions that significantly contributed to improve the paper. We thank the Ethiopian Space Science and Technology Institute (ESSTI) under the Ethiopian Ministry of Innovation and Technology (MOIT) for all the financial and technical supports. ZBA specially acknowledges Instituto de Radioastronomía Milimétrica (IRAM), Spain, for giving financial support and working space, and also extend thanks to Instituto de Astrofísica de Andalucía (IAA-CSIC), Spain, for providing a working space for part of the work. ZBA further extends special thanks to Joint ALMA Observatory (JAO) visitors' program for the financial and technical support during the data reduction. Moreover, ZBA acknowledges Kotebe Metropolitan University for granting a study leave and giving material supports. MP acknowledges support from the Spanish MCIU under project AYA2016-76682-C3-1-P, and from the State Agency for Research of the Spanish MCIU through the 'Center of Excellence Severo Ochoa' award for the Instituto de Astrofísica de Andalucía (SEV-2017-0709). MCS and APG are funded by Spanish State Research Agency grant MDM-2017- 0737 (Unidad de Excelencia María de Maeztu CAB). This work was supported by the Spanish Ministry of Economy and Competitiveness (MINECO) under the grants AYA2017-88007-C3-2-P. In this work, we made use of Virtual Observatory Tool for OPerations on Catalogues And Tables (TOPCAT), Python scientific codes, and IRAF. IRAF is distributed by the National Optical Astronomy Observatories, which are operated by the Association of Universities for Research in Astronomy, Inc., under cooperative agreement with the National Science Foundation. We also used ACS/*HST* data based on observations made with the NASA/ESA *HST*, and obtained from the Hubble Legacy Archive, which is a collaboration between the Space Telescope Science Institute (STScI/NASA), the Space Telescope European Coordinating Facility (ST-ECF/ESA), and the Canadian Astronomy Data centre (CADC/NRC/CSA).

DATA AVAILABILITY

The descriptions of the data underlying this article are available in the article and an online table as supplementary material.

REFERENCES

Alberts S. et al., 2014, MNRAS, 437, 437
Alberts S. et al., 2016, ApJ, 825, 72
Allen R. J., Kacprzak G. G., Glazebrook K., Tran K.-V. H., Spitler L. R., Straatman C. M. S., Cowley M., Nanayakkara T., 2016, ApJ, 826, 60
Alonso M. S., Lambas D. G., Tissera P., Coldwell G., 2007, MNRAS, 375, 1017
Altieri B. et al., 2010, A&A, 518, L17
Argudo-Fernández M., Lacerna I., Duarte Puertas S., 2018, A&A, 620, A113
Baldry I. K., Balogh M. L., Bower R. G., Glazebrook K., Nichol R. C., Bamford S. P., Budavari T., 2006, MNRAS, 373, 469
Baldwin J. A., Phillips M. M., Terlevich R., 1981, PASP, 93, 5
Balogh M. L., Morris S. L., Yee H. K. C., Carlberg R. G., Ellingson E., 1997, ApJ, 488, L75
Balogh M. L., Navarro J. F., Morris S. L., 2000, ApJ, 540, 113
Bertin E., Arnouts S., 1996, A&AS, 117, 393
Beyoro-Amado Z. et al., 2019, MNRAS, 485, 1528
Blanton M. R., Roweis S., 2007, AJ, 133, 734
Bongiovanni A., Bruzual G., Magris G., Gallego J., García-Dabó C. E., Coppi P., Sabbey C., 2005, MNRAS, 359, 930
Bongiovanni Á. et al., 2019, A&A, 631, A9
Bongiovanni Á. et al., 2020, A&A, 635, A35
Bornancini C., García D., 2020, MNRAS, 494, 1189
Bower R. G., Kodama T., Terlevich A., 1998, MNRAS, 299, 1193
Brinchmann J., Charlot S., White S. D. M., Tremonti C., Kauffmann G., Heckman T., Brinkmann J., 2004, MNRAS, 351, 1151
Brodwin M. et al., 2013, ApJ, 779, 138
Bruzual G., Charlot S., 2003, MNRAS, 344, 1000 (BC03)
Butcher H., Oemler A., 1984, ApJ, 285, 426
Cantale N. et al., 2016, A&A, 589, A82
Cepa J. et al., 2005, Rev. Mex. Astron. Astrofis. Ser. Conf., 24, 82
Chabrier G., 2003, PASP, 115, 763
Christlein D., Zabludoff A. I., 2005, ApJ, 621, 201
Chung S. M., Eisenhardt P. R., Gonzalez A. H., Stanford S. A., Brodwin M., Stern D., Jarrett T., 2011, ApJ, 743, 34
Cid Fernandes R. et al., 2015, MNRAS, 413, 1687
Coccato L. et al., 2020, MNRAS, 492, 2955
Coia D. et al., 2005, A&A, 430, 59
Cole D. et al., 2000, MNRAS, 319, 168
Cooper M. C. et al., 2008, MNRAS, 383, 1058
Cucciati O. et al., 2010, A&A, 520, A42
Cucciati O. et al., 2017, A&A, 602, A15
Czoske O., Kneib J.-P., Soucail G., Bridges T. J., Mellier Y., Cuillandre J.-C., 2001, A&A, 372, 391
Czoske O., Moore B., Kneib J.-P., Soucail G., 2002, A&A, 386, 31
Darvish B., Mobasher B., Sobral D., Rettura A., Scoville N., Faisst A., Capak P., 2016, ApJ, 825, 113

Downloaded from https://academic.oup.com/mnras/article/501/2/2430/6031334 by guest on 12 February 2026

Darvish B., Mobasher B., Martin D. C., Sobral D., Scoville N., Stroe A., Hemmati S., Kartaltepe J., 2017, ApJ, 837, 16
Davies R. I. et al., 2017, MNRAS, 466, 4917
Delaye L. et al., 2014, MNRAS, 441, 203
Deshev B. et al., 2017, A&A, 607, A131
Diaferio A., Geller M. J., Rines K. J., 2005, ApJ, 628, L97
Dressler A., 1980, ApJ, 236, 351
Dressler A., Thompson I. B., Shectman S. A., 1985, ApJ, 288, 481
Dressler A., Oemler A., Poggianti B. M., Gladders M. D., Abramson L., Vulcani B., 2013, ApJ, 770, 62
Džudžar R., Kilborn V., Murugeshan C., Meurer G., Sweet S. M., Putman M., 2019, MNRAS, 490, L6
Eastman J., Martini P., Sivakoff G., Kelson D. D., Mulchaey J. S., Tran K.-V., 2007, ApJ, 664, L9
Fasano G. et al., 2012, MNRAS, 420, 926
Fasano G. et al., 2015, MNRAS, 449, 3927
Filippenko A., Greenstein J. L., 1984, PASP, 96, 530
Gavazzi G., Savorgnan G., Fumagalli M., 2011, A&A, 534, A31
Geach J. E. et al., 2006, ApJ, 649, 661
Geach J. E., Smail I., Moran S. M., Treu T., Ellis R. S., 2009, ApJ, 691, 783
Gómez P. L. et al., 2003, ApJ, 584, 210
González J. J., Cepa J., González-Serrano J. I., Sánchez-Portal M., 2014, MNRAS, 443, 3289
Guglielmo V. et al., 2019, A&A, 625, A112
Gunn J. E., Gott J. R., III, 1972, ApJ, 176, 1
Haines C. P. et al., 2009, ApJ, 704, 126
Haines C. P. et al., 2013, ApJ, 775, 126
Hansen S. M. et al., 2009, ApJ, 699, 1333
Hora D. M., Xinyu D., 2020, AJ, 159, 69
Huertas-Company M., Rouan D., Tasca L., Soucail G., Le Fèvre O., 2008, A&A, 478, 971
Hwang H. et al., 2012, A&A, 538A, 15
Hwang H. S., Shin J., Song H., 2019, MNRAS, 489, 339
Ilbert O. et al., 2006, A&A, 457, 841
Jaffé Y. L., Smith R., Candlish G. N., Poggianti B. M., Sheen Y.-K., Verheijen M. A. W., 2015, MNRAS, 448, 1715
Jee M. J. et al., 2007, ApJ, 661, 728
Jones D. H., Shopbell P. L., Bland-Hawthorn J., 2002, MNRAS, 329, 759
Kauffmann G. et al., 2003, MNRAS, 346, 1055
Kauffmann G., White S. D. M., Heckman T. M., Ménard B., Brinchmann J., Charlot S., Tremonti C., Brinkmann J., 2004, MNRAS, 353, 713
Kelkar K., Gray M. E., Aragón-Salamanca A., Rudnick G., Jaffé Y. L., Jablonka P., Moustakas J., Milvang-Jensen B., 2019, MNRAS, 486, 868
Kennicutt R. C., Jr, 1992, ApJ, 388, 310
Kennicutt R. C., Jr, 1998, ARA&A, 36, 189
Kewley L. J., Dopita M. A., Sutherland R. S., Heisler C. A., Trevena J., 2001, ApJ, 556, 121
Kewley L. J., Groves B., Kauffmann G., Heckman T., 2006, MNRAS, 372, 961
Kewley L. J., Dopita M. A., Leitherer C., Davé R., Yuan T., Allen M., Groves B., Sutherland R., 2013, ApJ, 774, 100
Kneib J.-P. et al., 2003, ApJ, 598, 804
Kodama T., Bower R. G., 2001, MNRAS, 321, 18
Kodama T., Balogh M. L., Smail I., Bower R. G., Nakata F., 2004, MNRAS, 354, 1103
Koopmann R. A., Kenney J. D. P., 1998, ApJ, 497, L75
Koulouridis E., Bartalucci I., 2019, A&A, 623, L10
Kovač K. et al., 2014, MNRAS, 438, 717
Koyama Y. et al., 2008, MNRAS, 391, 1758
Koyama Y., Kodama T., Shimasaku K., Hayashi M., Okamura S., Tanaka I., Tokoku C., 2010, MNRAS, 403, 1611
Koyama Y., Kodama T., Nakata F., Shimasaku K., Okamura S., 2011, ApJ, 734, 66
Koyama Y. et al., 2013, MNRAS, 434, 423
Laganá T. F., Ulmer M. P., 2018, MNRAS, 475, 523
Lamareille F. et al., 2009, AA, 495, 53
Lara-López M. A. et al., 2010, PASP, 122, 1495
Larson R. B., Tinsley B. M., Caldwell C. N., 1980, ApJ, 237, 692
Le Fèvre O. et al., 2013, A&A, 559, A14
Li F. et al., 2019, MNRAS, 484, 3806
Lindegren L. et al., 2016, A&A, 595, A4
Lindegren L. et al., 2018, A&A, 616, A2
Maier C. et al., 2016, A&A, 590, A108
Marshall M. A., Shabala S. S., Krause M. G. H., Pimbblet K. A., Croton D. J., Owers M. S., 2018, MNRAS, 474, 3615
Martini P., Kelson D. D., Mulchaey J. S., Trager S. C., 2002, ApJ, 576, L109
Martini P. et al., 2013, ApJ, 768, 1
Marziani P. et al., 2017, A&A, 599, A83
Massey P., Gronwall C., 1990, ApJ, 358, 344
Matharu J. et al., 2020, MNRAS, 493, 6011
Miller C. J., Nichol R. C., Gómez P. L., Hopkins A. M., Bernardi M., 2003, ApJ, 597, 142
Moore B., Katz N., Lake G., Dressler A., Oemler A., 1996, Nature, 379, 613
Moran S. M., Ellis R. S., Treu T., Smail I., Dressler A., Coil A. L., Smith G. P., 2005, ApJ, 634, 977
Moran S. M., Ellis R. S., Treu T., Smith G. P., Rich R. M., Smail I., 2007, ApJ, 671, 1503
Muzzin A. et al., 2012, ApJ, 746, 188
Nantais J. B., Flores H., Demarco R., Lidman C., Rosati P., Jee M. J., 2013, A&A, 555, A5
Nantais J. B. et al., 2017, MNRAS, 465, L104
Natarajan P., Kneib J.-P., Smail I., Treu T., Ellis R., Moran S., Limousin M., Czoske O., 2009, ApJ, 693, 970
Nipoti C., Binney J., 2007, MNRAS, 382, 1481
Noeske K. G. et al., 2007, ApJ, 660, L43
Oh S. et al., 2018, ApJS, 237, 14
Oke J. B., 1974, ApJS, 27, 21
Oke J. B., 1990, AJ, 99, 1621
Oke J. B., Gunn J. E., 1983, ApJ, 266, 713
Old L. J. et al., 2020, MNRAS, 493, 5987
Patel S. G., Kelson D. D., Holden B. P., Franx M., Illingworth G. D., 2011, ApJ, 735, 53
Paulino-Afonso A., Sobral D., Darvish B., Ribeiro B., Stroe A., Best P., Afonso J., Matsuda Y., 2018, A&A, 620, A186
Peng Y.-. jie . et al., 2010, ApJ, 721, 193
Peng Y.-. jie ., Lilly S. J., Renzini A., Carollo M., 2012, ApJ, 757, 4
Pérez-Martínez J. M., Ziegler B., Böhm A., Verdugo M., 2020, A&A, 637, A30
Pimbblet K. A., Smail I., Kodama T., Couch W. J., Edge A. C., Zabludoff A. I., O'Hely E., 2002, MNRAS, 331, 333
Pimbblet K. A., Shabala S. S., Haines C. P., Fraser-McKelvie A., Floyd D. J. E., 2013, MNRAS, 429, 1827
Pintos-Castro I. et al., 2013, A&A, 558, A100
Pintos-Castro I. et al., 2016, A&A, 592, A108
Pintos-Castro I., Yee H. K. C., Muzzin A., Old L., Wilson G., 2019, ApJ, 876, 40
Poggianti B. M. et al., 2008, ApJ, 684, 888
Poggianti B. M. et al., 2017, ApJ, 844, 48
Pović M. et al., 2012, A&A, 541, 118
Pović M. et al., 2013, MNRAS, 435, 3444
Pović M. et al., 2015, MNRAS, 453, 1644
Press W. H., Schechter P., 1974, ApJ, 187, 425
Ramón-Pérez M. et al., 2019, A&A, 631, A10
Ramón-Pérez M. et al., 2019, A&A, 631, A11
Roediger E., 2009, Astron. Nachr., 330, 888
Rousselot P., Lidman C., Cuby J.-G., Moreels G., Monnet G., 2000, A&A, 354, 1134
Rudnick G. et al., 2017, ApJ, 850, 181
Sánchez-Portal M. et al., 2015, A&A, 578, A30
Saracco P., Gargiulo A., Ciocca F., Marchesini D., 2017, A&A, 597, A122
Schawinski K., Thomas D., Sarzi M., Maraston C., Kaviraj S., Joo S.-J., Yi S. K., Silk J., 2007, MNRAS, 382, 1415
Seaton M. J., 1979, MNRAS, 187, 73P
Sivakoff G. R., Martini P., Zabludoff A. I., Kelson D. D., Mulchaey J. S., 2008, ApJ, 682, 803

Downloaded from https://academic.oup.com/mnras/article/501/2/2430/6031334 by guest on 12 February 2026

Sobral D., Stroe A., Dawson W. A., Wittman D., Jee M. J., Röttgering H., van Weeren R. J., Brüggen M., 2015, MNRAS, 450, 630
Sobral D., Stroe A., Koyama Y., Darvish B., Calhau J., Afonso A., Kodama T., Nakata F., 2016, MNRAS, 458, 3443
Speagle J. S., Steinhardt C. L., Capak P. L., Silverman J. D., 2014, ApJS, 214, 15
Stasińska G., Costa-Duarte M. V., Vale Asari N., Cid Fernandes R., Sodré L., 2015, MNRAS, 449, 559
Stroe A. et al., 2015, MNRAS, 450, 646
Tiley A. L. et al., 2020, MNRAS, 496, 649
Tomczak A. R. et al., 2019, MNRAS, 484, 4695
Trager S. C., Worthey G., Faber S. M., Burstein D., González J. J., 1998, ApJS, 116, 1
Tran K.-V. H. et al., 2010, ApJ, 719, L126
Trenti M. et al., 2012, ApJ, 746, 55
Treu T., Ellis R. S., Kneib J.-P., Dressler A., Smail I., Czoske O., Oemler A., Natarajan P., 2003, ApJ, 591, 53
von den Bosch A. et al., 2008, MNRAS, 387, 79
von der Linden A., Wild V., Kauffmann G., White S. D. M., Weinmann S., 2010, MNRAS, 404, 1231
Vulcani B., Poggianti B. M., Finn R. A., Rudnick G., Desai V., Bamford S., 2010, ApJ, 710, L1
Vulcani B., Poggianti B. M., Fritz J., Fasano G., Moretti A., Calvi R., Paccagnella A., 2015, ApJ, 798, 52
Weinmann S. M., van den Bosch F. C., Yang X., Mo H. J., 2006, MNRAS, 366, 2
Wen Z. L., Han J. L., 2013, MNRAS, 436, 275
Whitmore B. C., Gilmore D. M., Jones C., 1993, ApJ, 407, 489

SUPPORTING INFORMATION

Supplementary data are available at *MNRAS* online.

Table A1. Example of the catalogue describing [O III] and H β emitters in ZwCl0024+1652 cluster.

Please note: Oxford University Press is not responsible for the content or functionality of any supporting materials supplied by the authors. Any queries (other than missing material) should be directed to the corresponding author for the article.

APPENDIX A: CATALOGUE OF [O III] AND/OR H β EMITTERS IN ZWCL0024+1652 GALAXY CLUSTER

A catalogue of emission line galaxies in ZwCl0024+1652 cluster is presented in this paper. Table A1 gives only an example, while

Table A1. Example of the catalogue describing [O III] and H β emitters in ZwCl0024+1652 cluster (Full catalogue is available online).

H α_ID	[O III]_ID	Hβ_ID	*HST*_ID	RA (deg)	DEC (deg)
R (Mpc)	z_[O III]	z_H β	z_H α	$f_{[O\,iii]}$	$f_{H\beta}$
$f_{H\alpha}$	$f_{[N\,ii]}$	EW_H β	Line_detected	log (M_*/M$_\odot$)	ELG_Type
BPT_class	Morpho_class	Morpho_source			
1015_O	−99	1009_O	−99	6.6232	17.2470
2.8131	99.	0.3955	0.3937	−99.	1.4467
4.6594	1.3600	5.1800	H β,H α,[N II]	9.9446	SF
99.9	99.9	99.9	–	–	–
1039_O	−99	946_O	136	6.5373	17.2530
4.5367	99.	0.3959	0.3961	−99.	0.7424
2.8236	2.2306	2.1550	H β,H α,[N II]	10.8850	BLAGN
99.9	ET	A,B	–	–	–
1057_O	1056_O	−99	−99	6.5649	17.2297
1.8003	0.3922	99.	0.3934	0.2523	−99.
1.3030	0.4714	−99.	[O III],H α,[N II]	9.9831	SF
99.9	99.9	99.9	–	–	–
1097_O	1068_O	1203_O	−99	6.6542	17.2282
3.6278	0.3957	0.3954	0.3947	0.2044	0.2124
0.8933	0.4282	4.3030	H β,[O III],H α,[N II]	9.2247	SF
composite	99.9	99.9			
1157_O	1134_O	1306_O	109	6.5377	17.2212
4.1462	0.4057	0.4039	0.4042	1.2396	1.3597
5.3748	0.9067	3.976	H β,[O III],H α,[N II]	10.4082	SF
SF	LT	A	–	–	–
1173_O	810_O	902_O	−99	6.6182	17.2600
3.1621	0.3876	0.3917	0.3901	0.6628	0.6482
1.7725	0.5727	5.226	H β,[O III],H α,[N II]	9.0650	SF
SF	99.9	99.9	–	–	–

Downloaded from https://academic.oup.com/mnras/article/501/2/2430/6031334 by guest on 12 February 2026

the full catalogue will be given in the electronic version of paper. Properties of [O III] and Hβ emission lines are given for 35 and 59 galaxies, respectively. We added also the data of [NII] and Hα emitters studied in Sánchez-Portal et al. (2015). The entire catalogue gives the following properties of 73 galaxies:

Column 1 ... Hα line ID number with subscript O for offset and C for centre position;

Column 2 ... [O III] line ID number with subscript O for offset and C for centre position; $= -99$ if not available;

Column 3 ... Hβ line ID number with subscript O for offset and C for centre position; $= -99$ if not available;

Column 4 ... *HST* ID number; $= -99$. if not available;

Column 5 ... Right Ascension in decimal degrees (J2000);

Column 6 ... Declination in decimal degrees (J2000);

Column 7 ... Clustercentric distance in Mpc;

Column 8 ... TF redshift measured with [O III] line; $= 99$. if not available;

Column 9 ... TF redshift measured with Hβ line; $= 99$. if not available;

Column 10 ... TF redshift measured with Hα line; $= 99$. if not available;

Column 11 ... [O III] flux in $\times 10^{-16}$ erg s^{-1} cm^{-2}; $= -99$. if not available;

Column 12 ... Hβ flux in $\times 10^{-16}$ erg s^{-1} cm^{-2}; $= -99$. if not available;

Column 13 ... Hα flux in $\times 10^{-16}$ erg s^{-1} cm^{-2}; $= -99$. if not available;

Column 14 ... [N II] flux in $\times 10^{-16}$ erg s^{-1} cm^{-2}; $= -99$. if not available;

Column 15 ... Hβ equivalent width in Å; $= -99$. if not available;

Column 16 ... List of emission lines detected;

Column 17 ... Base 10 logarithm of stellar mass, log (M_*/M$_\odot$); $= -99$. if not available;

Column 18 ... Emission line galaxy (ELG) type based on Sánchez-Portal et al. (2015);

Column 19 ... BPT-NII classification; $= -99.9$ if not available;

Column 20 ... Broad morphological class, early-type (ET) or late-type (LT); 99.9 if not available;

Column 21 ... ource of the morphological class (A = Treu et al. (2003), B = Moran et al. (2007), C = Beyoro-Amado et al. (2019)); 99.9 if not available;

This paper has been typeset from a TEX/LATEX file prepared by the author.

Downloaded from https://academic.oup.com/mnras/article/501/2/2430/6031334 by guest on 12 February 2026